CANCER

Oncogenic transcription factors instruct promoter-enhancer hubs in individual triple negative breast cancer cells

Jingru Zhao[1,2,3], Yeqiao Zhou[1,2,3], Ilias Tzelepis[1,2,3], Noah G. Burget[1,2,3], Junwei Shi[2,3,4], Robert B. Faryabi[1,2,3]*

Sequencing-based mapping of ensemble pairwise interactions among regulatory elements support the existence of topological assemblies known as promoter-enhancer hubs or cliques in cancer. Yet, prevalence, regulators, and functions of promoter-enhancer hubs in individual cancer cells remain unclear. Here, we systematically integrated functional genomics, transcription factor screening, and optical mapping of promoter-enhancer interactions to identify key promoter-enhancer hubs, examine heterogeneity of their assembly, determine their regulators, and elucidate their role in gene expression control in individual triple negative breast cancer (TNBC) cells. Optical mapping of individual *SOX9* and *MYC* alleles revealed the existence of frequent multiway interactions among promoters and enhancers within spatial hubs. Our single-allele studies further demonstrated that lineage-determining SOX9 and signaling-dependent NOTCH1 transcription factors compact *MYC* and *SOX9* hubs. Together, our findings suggest that promoter-enhancer hubs are dynamic and heterogeneous topological assemblies, which are controlled by oncogenic transcription factors and facilitate subtype-restricted gene expression in cancer.

INTRODUCTION

The spatial organization of the genome facilitates communication between promoters and enhancers, a process that is crucial for the regulation of oncogenic transcriptional programs (*1*). Emerging evidence from studies in nonmalignant cells supports that multiple enhancers and promoters could spatially coalesce, forming topological assemblies that are variably referred to as promoter-enhancer hubs, multi-enhancer hubs, or three-dimensional (3D) cliques (*2–4*). The presence of promoter-enhancer hubs and their association with aberrant transcription have also been reported in malignant cell populations (*5–7*); yet, the organizational principles, regulators, and functions of these topological assemblies in cancer are not well understood.

Biochemical proximity ligation-based chromatin conformation capture (3C) methods, including Hi-C, have enabled genome-wide examination of long-range pairwise promoter-enhancer interactions in cancer genomes (*8–13*). By examining the ensemble behavior of millions of cancer cells, 3C-based studies attest to the formation of promoter-enhancer hubs within a population of cancer cells and linked them to aberrant gene expression control (*5, 6*). However, population-based studies can only examine the average of all pairwise promoter-enhancer interactions and cannot distinguish between co-occurring interactions in the same cells and mutually exclusive interactions occurring in different cells. To overcome this limitation, various 3C protocol variants (e.g., multi-contact 4C) and methods without proximity ligation (e.g., split-pool recognition of interactions by tag extension) were developed, revealing the existence of multiway interactions between promoters and enhancers in nonmalignant cells (*14, 15*). Despite these recent advances, the prevalence of multiway interactions and the organizational principles of promoter-enhancer hubs in individual cancer cells remain unclear.

Mapping of pairwise promoter-enhancer interactions in cancer cell populations suggested that rewiring of promoter-enhancer hubs is associated with deregulation of transcription factors and coactivators (*5–7, 16–18*). Nevertheless, ensemble mapping of promoter-enhancer interactions provides limited information on the underlying mechanisms driving variability and heterogeneity of pairwise and multiway interactions between regulatory elements in individual cancer cells, raising the question of how promoter-enhancer hubs are regulated.

Here, we used triple-negative breast cancer (TNBC) as a model to investigate the organizational principles, regulators, and functions of promoter-enhancer hubs. TNBC is a highly aggressive subtype of breast cancer, characterized by the absence of progesterone and estrogen receptors (ER) and the lack of human epidermal growth factor receptor 2 amplification or overexpression (*19*). To identify and examine key promoter-enhancer hubs in TNBC, we integrated data from functional genomics, transcription factor screening, and optical mapping of multiway promoter-enhancer interactions. Our studies demonstrated that hyper-interacting promoter-enhancer hubs in TNBC are predominantly located at loci encoding oncogenic transcription factors essential for cancer growth, including *SOX9* and *MYC*. Optical mapping of *SOX9* and *MYC* hyper-interacting loci in each individual TNBC cell revealed that these two oncogenes are regulated by multiple distally located enhancer clusters that cooperatively participate in frequent pairwise and multiway interactions with their respective gene promoter. Our single-allele studies further revealed that enhancer activity, SOX9 and NOTCH1 chromatin binding, as well as Notch transcription complex (NTC) activity compact *MYC* and *SOX9* promoter-enhancer hubs in individual TNBC cells. Together, our single-cell/single-allele resolution studies in TNBC suggest that formation of promoter-enhancer hubs is an additional epigenetic mechanism hijacked by oncogenic transcription factors to promote aberrant gene expression.

[1]Department of Pathology and Laboratory Medicine, University of Pennsylvania Perelman School of Medicine, Philadelphia, PA 19104, USA. [2]Penn Epigenetics Institute, University of Pennsylvania Perelman School of Medicine, Philadelphia, PA 19104, USA. [3]Abramson Family Cancer Research Institute, University of Pennsylvania Perelman School of Medicine, Philadelphia, PA 19104, USA. [4]Department of Cancer Biology, University of Pennsylvania, Philadelphia, PA 19104, USA.
*Corresponding author. Email: faryabi@pennmedicine.upenn.edu

RESULTS

SOX9 resides in one of the most hyper-interacting promoter-enhancer hubs in TNBC

To identify ensemble promoter-enhancer hubs in TNBC, we first used population-based assays to create a genome-wide map of highly interacting enhancers and promoters. We integrated high-resolution cohesin subunit SMC1 HiChIP and histone mark mapping in TNBC MB157 (*6*) and algorithmically searched for groups of densely interacting enhancers and promoters, under the assumption that promoter-enhancer hubs participate in frequent intragroup and infrequent intergroup pairwise interactions at the population level (see Materials and Methods). We observed a substantial asymmetry in the pairwise interactivity distribution of promoter-enhancer hubs

(Fig. 1A). A small fraction of active enhancer and promoter elements converged into the 136 "hyper-interacting" promoter-enhancer hubs detected in TNBC MB157 (see Materials and Methods), suggesting that hubs could potentially contribute to regulation of genes critical for TNBC oncogenesis.

Interrogation of genes within hyper-interacting promoter-enhancer hubs showed that they are predominantly involved in chromatin binding and transcription regulation activities (fig. S1A). To test the hypothesis that hyper-interacting promoter-enhancer hubs may contain transcription factors essential to TNBC survival, we conducted DNA binding domain–focused CRISPR-Cas9 screens. TNBC MB157 and MDA-MB-468 cells stably expressing Cas9 were transduced with a pooled library containing 8658 single guide RNAs
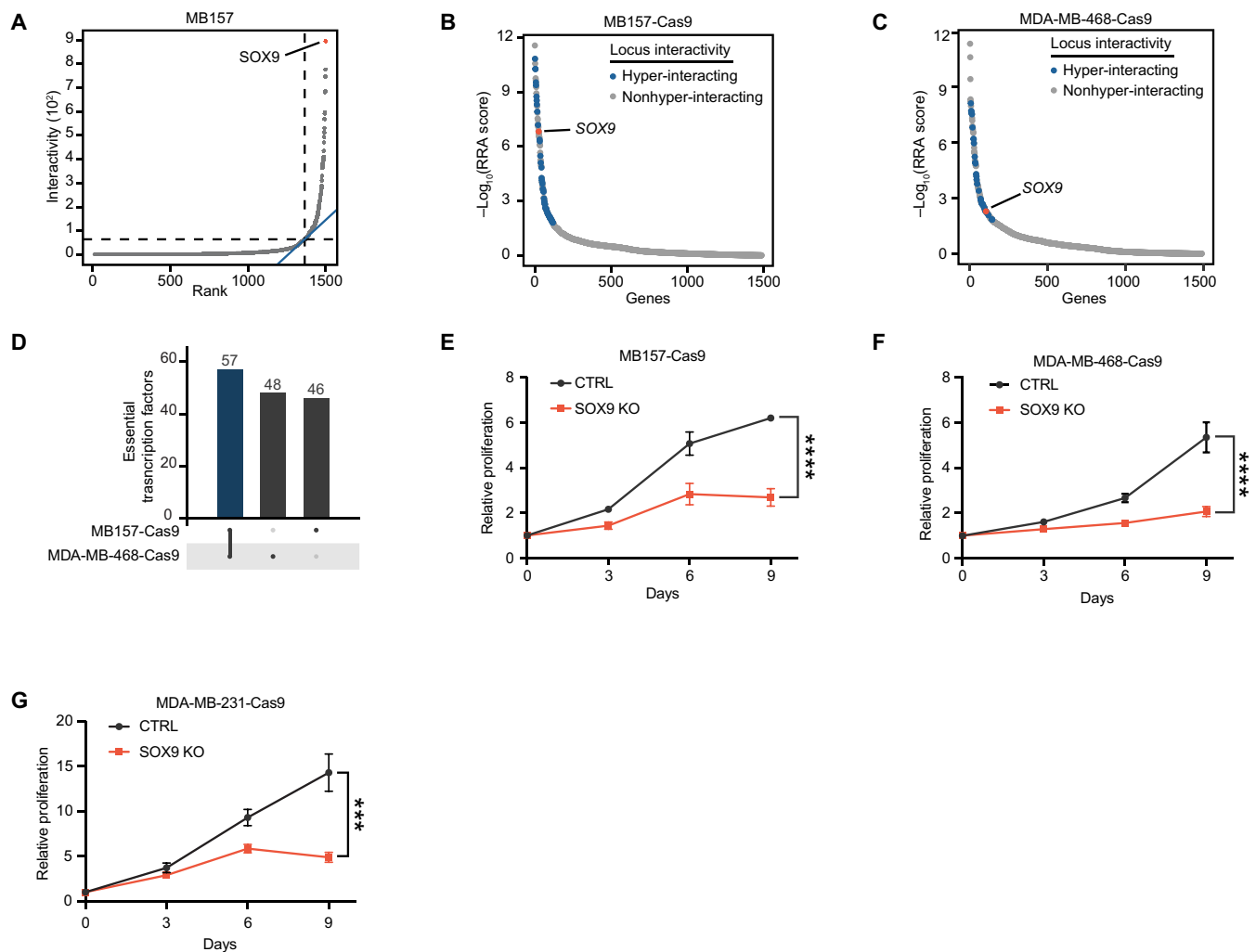
Fig. 1. *SOX9* is essential for TNBC proliferation and resides in one of the most hyper-interacting promoter-enhancer hubs. (**A**) *SOX9* resides in the most hyper-interacting TNBC MB157 promoter-enhancer hub. MB157 hubs plotted in ascending order of their total connectivity as measured by SMC1 HiChIP in TNBC MB157. Hyper-interacting promoter-enhancer hubs are defined as the ones above the elbow of the ranked total connectivity plot. *SOX9* hyper-interacting promoter-enhancer hub is marked in red. (**B** and **C**) Domain-focused CRISPR screens of 1486 transcription factors identify *SOX9* as an essential gene in TNBC MB157 (B) and MDA-MB-468 (C). Genes are ranked based on MAGeCK Robust Rank Aggregation (RRA) score for negative selection. A smaller RRA score indicates stronger negative selection of the corresponding gene. Essential genes residing in hyper-interacting promoter-enhancer hubs are indicated with colored dots, including *SOX9*. Essentiality significance: *P* value < 0.05. (**D**) Fifty-seven essential transcription factors are shared between TNBC MB157 and MDA-MB-468. Upset plot of essential and expressed transcription factors from transcription factor CRISPR screen in MB157 and MDA-MB-468. (**E** to **G**) Loss of SOX9 significantly reduces growth of TNBC. Relative cell growth (CellTiter-Glo) was tracked for 9 days in Cas9-expressing TNBC MB157 (E) MDA-MB-468 (F) MDA-MB-231 (G) cells after transduction with control sgRNA (CTRL) or SOX9-targeting sgRNA [SOX9 knockout (KO)]. CellTiter-Glo day 0 are 4 days post-sgRNA transduction. *N* = 5 technical replicates. *t* test: *P < 0.05, **P < 0.01, ***P < 1×10^{-3}, and ****P < 1×10^{-4}.

(sgRNAs) targeting 1427 transcription factors and control genes. Positive and negative control sgRNAs validated the overall accuracy of the screening approach (fig. S1, B to E, and table S1). Integration of data from negative selection "dropout" screens and transcriptomics showed that 103 and 105 transcription factors were expressed and essential for MB157 and MDA-MB-468 proliferation, respectively (Fig. 1, B and C). Notably, 23 of 57 genes essential for both MB157 and MDA-MB-468 resided in hyper-interacting promoter-enhancer hubs (Fig. 1, B to D, and table S1) and were among the ER-negative (ER⁻)/TNBC signature gene sets (fig. S1F). Comparison with DepMap CRISPR screen data across cell lines representing various breast cancer subtypes revealed that some essential genes within hyper-interacting hubs, such as *MYC*, are indispensable across all subtypes, while others, such as *SOX9*, exhibit selective essentiality specifically in TNBC (fig. S1, G and H). Together, these data suggest that essential transcription factors in TNBC may be preferentially regulated by promoter-enhancer hubs.

We observed that *SOX9* resides in the most hyper-interacting promoter-enhancer hub (Fig. 1A) and was deemed essential for TNBC MB157 and MDA-MB-468 by dropout CRISPR-Cas9 screen (Fig. 1, B and C). SOX9 is a lineage-determining transcription factor during normal differentiation of ER⁻ luminal stem/progenitor epithelial cells (*20–22*), which are thought to be the cells of origin for TNBC (*23–26*). SOX9 has also been implicated as a key member of multiple oncogenic pathways (fig. S1F) (*22, 27*). Concordantly, CRISPR-Cas9–mediated genetic deletion of *SOX9* markedly impaired proliferation of TNBC MB157, MDA-MB-468, and MDA-MB-231 (Fig. 1, E to G, and fig. S1I). Conversely, ER-expressing (ER⁺) breast cancer cells expressed a lower level of SOX9 and exhibited SOX9-invariant proliferation (fig. S1, I and J), consistent with the SOX9 independence of normal ER⁺ luminal progenitor cells (*20*). In tandem with these data, transcriptomic analysis of primary samples further showed elevated *SOX9* expression levels in TNBC tumors compared to matched normal tissue and tumors from other breast cancer subtypes (fig. S1, K and L). These data collectively support the TNBC-restricted expression and surmise the potential oncogenic function of the *SOX9* hyper-interacting promoter-enhancer hub.

Subtype-restricted distal enhancer clusters promote SOX9 expression in TNBC

Although SOX9 hyperactivation plays a pivotal role in TNBC tumorigenesis, the mechanisms underpinning its aberrant transcriptional regulation remains unclear (*27*). To determine how *SOX9* exhibits subtype-restricted expression, we examined the chromatin activity of the *SOX9* locus in TNBC and ER⁺ breast cancer. This analysis identified three putative enhancer clusters (EC) with high levels of chromatin accessibility and active enhancer mark H3K27ac located 3′ of the *SOX9* promoter in TNBC MB157, MDA-MB-468, and MDA-MB-231, but not ER⁺ MCF7 and LTED (Fig. 2A and fig. S2, A to D). The smallest and most proximal putative enhancer cluster, which we referred to as *SOX9*.EC1, was located 280 kb 3′ of the *SOX9* promoter and spanned a 35-kb region; the second TNBC-restricted putative enhancer cluster, *SOX9*.EC2, was located 330 kb downstream of *SOX9* and spanned a 47-kb region. The largest and most distal putative enhancer cluster, *SOX9*.EC3, occupied a 102-kb region and was located 413 kb 3′ from the *SOX9* promoter. Notably, *SOX9*.EC1 and *SOX9*.EC2 genomic elements were also highly acetylated in human primary luminal progenitor cells, further supporting their potential role as lineage-restricted *SOX9* enhancer clusters

(Fig. 2A). Analysis of whole-genome sequencing data reveals that structural variants in this locus are prevalent among patients with breast cancer (*28*), suggesting that alterations in genome integrity during cancer transformation may induce the up-regulation of these potential enhancers and the emergence of novel ones.

To test whether elements within *SOX9*.EC1, *SOX9*.EC2, and *SOX9*.EC3 are TNBC-restricted *SOX9* enhancers, we used dCas9-KRAB (*29, 30*) to epigenetically silence individual elements within each putative enhancer cluster and examined expression of *SOX9*. As enhancers are found in nucleosome-free regions, we designed sgRNAs to target individual accessible elements flanked by high levels of H3K27ac in MB157, MDA-MB-231, and MDA-MB-468 cells (fig. S2, A to D). Notably, this approach led to precise recruitment of dCas9-KRAB, decrease in H3K27ac, and increase in H3K9me3 in the targeted elements without any off-target effect at the *SOX9* locus (fig. S2E). Targeting a prominent element within *SOX9*.EC1 in dCas9-KRAB–expressing MB157, MDA-MB-231 and MDA-MB-468 TNBC cells reduced *SOX9* expression by 39, 33, and 31% across four biological replicates, respectively (Fig. 2B). Similar to *SOX9*.EC1, inactivation of a highly acetylated element within *SOX9*.EC2 significantly down-regulated *SOX9* in all three cell lines, with MB157, MDA-MB-231, and MDA-MB-468 having 38, 58, and 43% reduction in *SOX9* expression, respectively (Fig. 2C). We additionally investigated the function of the *SOX9*.EC3 cluster of putative enhancers by targeting a genomic element active in all three TNBC models. These studies showed that an element within *SOX9*.EC3 functions as a *SOX9* enhancer, as its inactivation reduced *SOX9* expression by 37, 46, and 43% in MB157, MDA-MB-231, and MDA-MB-468, respectively (Fig. 2D). In contrast to TNBC, elements within *SOX9*.EC1, *SOX9*.EC2, and *SOX9*.EC3 were not functioning as enhancers in ER⁺ breast cancer MCF7 cells, as their inactivation did not markedly reduce expression of *SOX9* (Fig. 2, B to D). Together, these data exhibit that genomic elements within *SOX9*.EC1, *SOX9*.EC2, and *SOX9*.EC3 are potentially TNBC-restricted *SOX9* enhancers.

To further assess the functional significance of these *SOX9* enhancers, we examined their contribution to TNBC proliferation. Inactivation of elements within *SOX9*.EC1, *SOX9*.EC2, and *SOX9*. EC3 significantly and reproducibly reduced proliferation of TNBC MB157, MDA-MB-231, and MDA-MB-468 cells (Fig. 2, E to G, and fig. S2, F to J). Notably, even 31% reduction in *SOX9* expression upon inactivation of an enhancer within *SOX9*.EC1 was sufficient to markedly decrease MDA-MB-468 growth (Fig. 2G and fig. S2, I and J). In line with subtype-restricted activity of *SOX9* and its enhancers, targeting elements in *SOX9*.EC1, *SOX9*.EC2, and *SOX9*.EC3 with dCas9-KRAB had no significant impact on proliferation of ER⁺ MCF7 cells (Fig. 2H). Thus, our data show that TNBC proliferation uniquely depends on high *SOX9* expression that is promoted by three subtype-restricted enhancers.

The *SOX9* promoter and enhancers spatially coalesce in individual TNBC cells, forming promoter-enhancer hubs

Population-based SMC1 HiChIP data indicated that the *SOX9* promoter and its three TNBC-restricted enhancer clusters participate in frequent pairwise spatial interactions (Fig. 1A and fig. S3, A and B), raising the question whether these regulatory elements are also engaged in multiway interactions and form promoter-enhancer hubs in individual TNBC cells. To identify promoter-enhancer hubs at single-cell/single-allele resolution, we used Oligopaint DNA fluorescence in situ hybridization (FISH) with 3D confocal microscopy
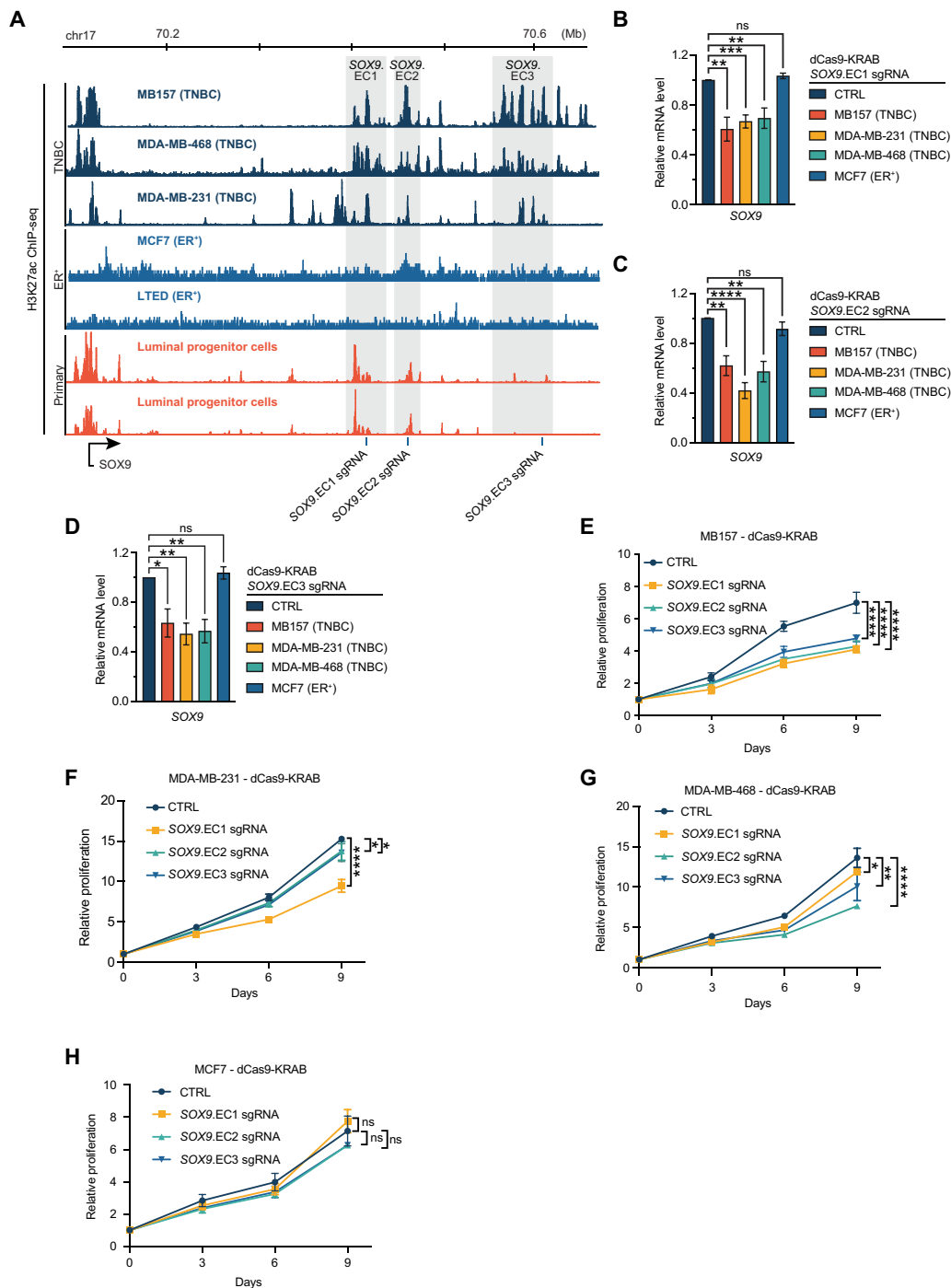
Fig. 2. Subtype-restricted distal enhancer clusters drive *SOX9* expression in TNBC. (**A**) Enrichment of active histone mark H3K27ac 3′ of *SOX9* at gray box-marked genomic regions *SOX9*.EC1, *SOX9*.EC2, and *SOX9*.EC3 in TNBC but not ER⁺ breast cancer cells. Tracks from top to bottom: H3K27ac ChIP-seq in TNBC MB157, MDA-MB-468, and MDA-MB-231, ER⁺ MCF7 and LTED, and TNBC cell-of-origin primary luminal progenitor cells from human donors. Blue lines represent the position of sgRNA-targeted sequences. (**B** to **D**) dCas9-KRAB experiments show that elements within highly acetylated *SOX9*.EC1, *SOX9*.EC2, and *SOX9*.EC3 are functional *SOX9* enhancers in TNBC but not ER⁺ cells. Bar plots showing normalized expression of *SOX9* in dCas9-KRAB–expressing TNBC MB157, MDA-MB-231, and MDA-MB-468 and ER⁺ MCF7 after inhibition of marked elements within *SOX9*.EC1 (B), *SOX9*.EC2 (C), and *SOX9*.EC3 (D) with noted sgRNAs relative to control sgRNA (CTRL) 6 days post-sgRNA transduction. Each condition is normalized to its corresponding CTRL sgRNA experiment. Data represent $N = 4$ biological replicates and presented as mean ± SEM. t test: $*P < 0.05$, $**P < 0.01$, $***P < 1 \times 10^{-3}$, and $****P < 1 \times 10^{-4}$. (**E** to **H**) Activity of enhancers within *SOX9*.EC1, *SOX9*.EC2, and *SOX9*.EC3 promote proliferation of TNBC but not ER⁺ cells. Relative cell growth (CellTiter-Glo) was tracked for 9 days in dCas9-KRAB–expressing TNBC MB157 (E) and MDA-MB-231 (F) MDA-MB-468 (G) and MCF7 (H) after transduction with CTRL, *SOX9*.EC1, *SOX9*.EC2, or *SOX9*.EC3 targeting sgRNA. $N = 5$ technical replicates. Data presented as mean ± SEM t test: $*P < 0.05$, $**P < 0.01$, $***P < 1 \times 10^{-3}$, and $****P < 1 \times 10^{-4}$. ns, not significant.

to calculate the 3D distance between the *SOX9* promoter and its three enhancer clusters in individual alleles. We also examined frequency of pairwise and multiway interactions among the regulatory elements by determining intraprobe 3D distances that were less than 350 nm, which has been shown to capture the link between promoter-enhancer physical proximity and productive transcription (*31*, *32*). These studies revealed that the single-allele frequency of pairwise *SOX9* promoter interaction with *SOX9*.EC1, *SOX9*.EC2, and *SOX9*.EC3 was 42.0, 37.9, and 20.5 to 21.9%, respectively (Fig. 3, A and B). Notably, both single-allele 3D Oligopaint DNA FISH and population-based SMC1 HiChIP data concordantly showed that the *SOX9* promoter less frequently interacts with *SOX9*.EC3 than with *SOX9*.EC1 or *SOX9*.EC2 (fig. S3A). These observations suggest that the ensemble sequencing data represent an average of differences in promoter-enhancer interaction frequency in individual cells and further support that looping interactions decrease with increased genomic distance (*33*).

The single-allele nature of 3D Oligopaint DNA FISH allowed us to investigate not only pairwise but also multiway interactions between the *SOX9* promoter and its three enhancer clusters. To this end, we separately measured 3D distances and frequency of interactions among the *SOX9* promoter, *SOX9*.EC1, and *SOX9*.EC3 (referred to as *SOX9*-EC1-EC3 hub), as well as the *SOX9* promoter, *SOX9*.EC2, and *SOX9*.EC3 (referred to as *SOX9*-EC2-EC3 hub) (Fig. 3, A and B). Of note, *SOX9*.EC1 and *SOX9*.EC2 are located approximately 15 kb apart, which technically hindered our ability to perform similar analyses to examine three-way interactions among *SOX9*.EC1, *SOX9*.EC2, and the *SOX9* promoter. Examination of more than 1000 individual alleles in MB157 showed that *SOX9*-EC1-EC3 and *SOX9*-EC2-EC3 three-way interactions were almost equally frequent and observed at 10.9 and 10.3% of alleles, respectively (Fig. 3, A and B). The *SOX9* promoter-enhancer hub was observed even more frequently in MDA-MB-468, with 22.6% of alleles having *SOX9*-EC1-EC3 three-way interactions (fig. S3C). Thus, in concordance with observations in nonmalignant cells (*34*), multiway interactions are relatively rare and occur in 10 to 20% of the TNBC *SOX9* alleles at any given time, which provides further evidence in support of the dynamic nature of spatial hubs.

Enhancer activity compacts *SOX9* promoter-enhancer hubs
Intrigued by observing multiway promoter-enhancer interactions in individual TNBC cells, we sought to investigate the underpinning mechanisms of *SOX9* spatial hub formation. Decrease in H3K27ac level is linked to loss of promoter-enhancer interactions without affecting topologically associated domains (TADs) and sub-TADs (*35*). Conversely, promoter-enhancer interactions can be altered independent of enhancer activity changes (*6*, *36–38*). To untangle the effect of enhancer activity on the topology of the *SOX9* locus, we leveraged dCas9-KRAB to inactivate elements within each of the *SOX9* enhancer clusters and measured promoter-enhancer distances in individual TNBC cells (Fig. 3, C to H, and fig. S3, D to O). Inactivation of each enhancer significantly increased the distance between the *SOX9* promoter and the inhibited enhancer (fig. S3, D, I, and N). Inactivation of *SOX9*.EC1 and *SOX9*.EC2 led to the most profound changes in promoter-enhancer proximity, with 191-nm increase in *SOX9*-EC1 and 185-nm increase in *SOX9*-EC2 mean distances, respectively. Together, these observations suggest that the activity of *SOX9* enhancers is closely linked to their spatial positioning.

Notably, our data also revealed that, in addition to the targeted enhancer cluster, inactivation of one enhancer repositioned the other two nontargeted enhancer clusters (fig. S3, E, F, H, J, L, and M). Following *SOX9*.EC1 inactivation, the number of cells with *SOX9* to *SOX9*.EC2 or *SOX9* to *SOX9*.EC3 interacting alleles decreased by 25 and 33.6%, respectively (fig. S3G). Similarly, dCas9-KRAB–mediated *SOX9*.EC2 inactivation decreased the number of cells with *SOX9* to *SOX9*.EC1 and *SOX9* to *SOX9*.EC3 interactions by 35.9 and 41.6%, respectively (fig. S3K). The same was observed when we inactivated *SOX9*.EC3, where the number of cells with *SOX9* to *SOX9*.EC1 or *SOX9* to *SOX9*.EC2 interactions decreased by 21.2 and 12.6%, respectively (fig. S3O). In tandem with changes in promoter-enhancer interaction frequency, we observed significant separation of the *SOX9* promoter from nontargeted enhancers (fig. S3, E, F, H, J, L, and M), suggesting that activity of one enhancer can affect the positioning of other enhancers within *SOX9* promoter-enhancer hubs.

To determine whether decreases in *SOX9* promoter-enhancer interaction frequency translates to topological changes in the *SOX9* hub, we calculated the spatial perimeter, defined as the sum of the 3D Euclidean distances between the *SOX9* promoter to *SOX9*.EC1, *SOX9*.EC1 to *SOX9*.EC3, and *SOX9* promoter and *SOX9*.EC3 for each allele, before and after targeting each enhancer. Examination of more than 1000 cells per condition showed that *SOX9*.EC1, *SOX9*.EC2, and *SOX9*.EC3 inactivation markedly increased the spatial perimeter of *SOX9* promoter, *SOX9*.EC1, and *SOX9*.EC3 (Fig. 3C). Concordant with the expansion of the spatial perimeter, targeting each enhancer reduced the frequency of alleles with *SOX9*-EC1-EC3 three-way interactions by 59.0% (Fig. 3, D and E). Similarly, examination of the *SOX9* promoter, *SOX9*.EC2, and *SOX9*.EC3 spatial perimeters and three-way interactions showed that targeting each enhancer expands the *SOX9* promoter-enhancer hub (Fig. 3F) and decreases the frequency of cells with three-way interaction among these genomic elements (Fig. 3, G and H). Thus, the activity of one enhancer can determine the topology and frequency of multiway interactions among all enhancers and the promoter within the *SOX9* spatial hub.

To determine whether the activity of the promoter also influences *SOX9* promoter-enhancer hub compaction, we inhibited the *SOX9* promoter using dCas9-KRAB (fig. S2K) and assessed interactions between the *SOX9* promoter, *SOX9*.EC1, and *SOX9*.EC3. Targeting the *SOX9* promoter reduced three-way interactions by 43.8%, concordant with significant expansion of the *SOX9*-EC1-EC3 spatial perimeter (Fig. 3I), indicating that the activity of both enhancers and promoters contributes to spatial organization of *SOX9* hubs.

Notch transcription complex chromatin binding positions *SOX9* enhancers
Signaling-dependent Notch transcription factor is a key regulator of cell fate decision in a variety of cell types, including mammary epithelial cells (*39–42*). Notch and SOX9 are both highly expressed and maintain the ER⁻ lineage of luminal progenitor epithelial cells (*20*, *21*, *43*, *44*), which are likely TNBC's cells of origin (*23–26*). Given that oncogenic Notch contributes to TNBC pathogenesis and genome folding (*6*, *45*, *46*), we postulated that Notch contributes to multiway interactions and compaction of the *SOX9* promoter-enhancer hub.

Mapping of the three components of NTC—nuclear NOTCH1 intracellular domain (NICD1), DNA binding protein recombination signal binding protein for immunoglobulin kappa J region (RBPJ),
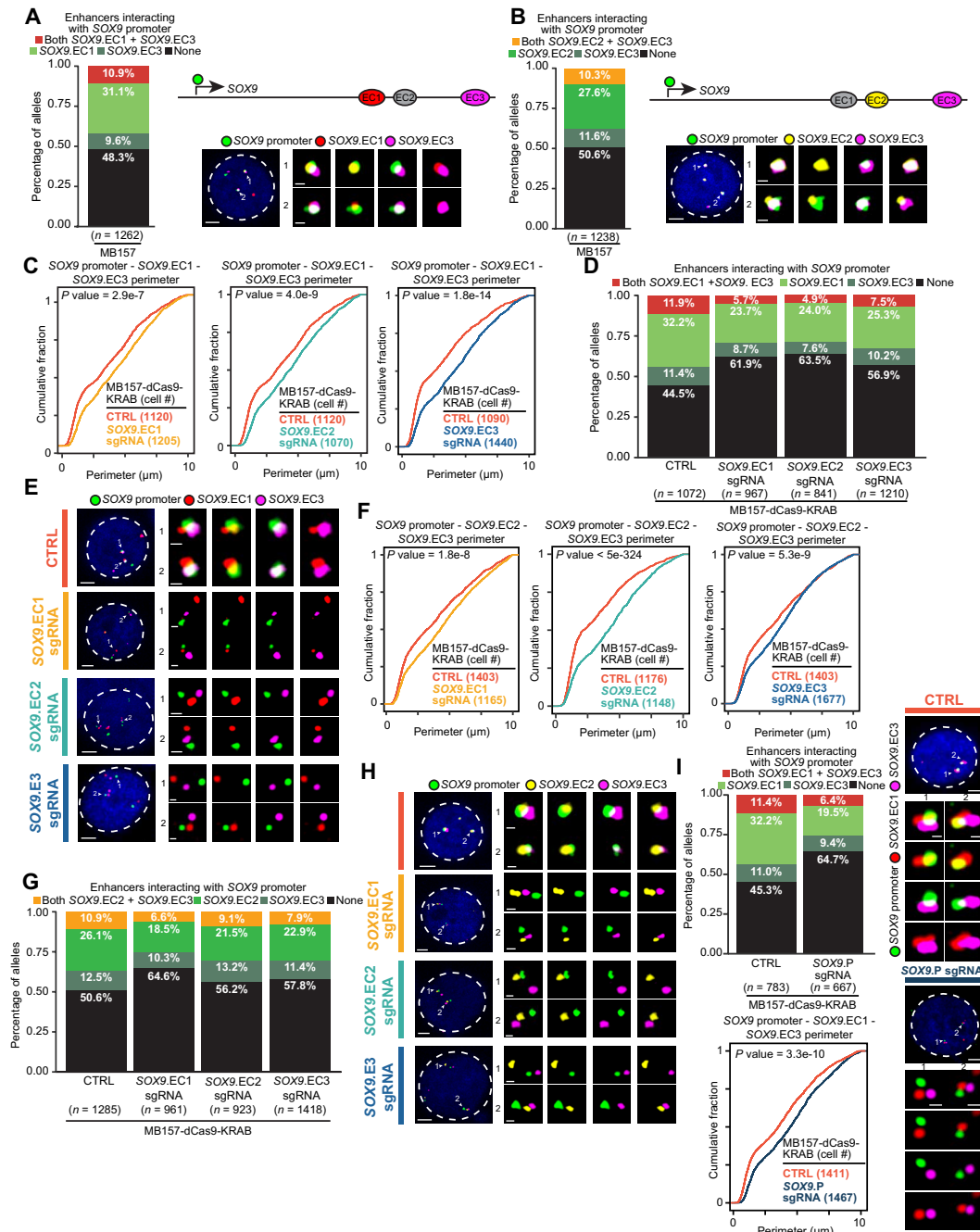
Fig. 3. Enhancer activity compacts *SOX9* promoter-enhancer hub in individual TNBC cells. (**A** and **B**) *SOX9* promoter participates in multiway interactions with its distal enhancer clusters in individual TNBC MB157 cells. Left: Allele percentages with *SOX9* promoter interacting with *SOX9*.EC1, *SOX9*.EC3, or both (A) and *SOX9*.EC2, *SOX9*.EC3, or both (B) in MB157 (*n* = alleles). Right-top: *SOX9* locus schematic, three-color DNA FISH 50-kb probes at *SOX9* promoter (green), *SOX9*.EC3 (magenta), and *SOX9*.EC1 (A, red) or *SOX9*.EC2 (B, yellow). Locations per fig. S3A. Right-bottom: Representative cells. Blue: 4′,6-Diamidino-2-phenylindole (DAPI). (**C** and **F**) *SOX9* enhancers inactivation expands *SOX9*-EC1-EC3 and *SOX9*-EC2-EC3 hubs in individual TNBC MB157 cells. Cumulative distribution functions (CDFs) of *SOX9*-EC1-EC3 (C) and *SOX9*-EC2-EC3 (F) spatial perimeters in each MB157–dCas9-KRAB expressing control (CTRL), *SOX9*.EC1, *SOX9*.EC2, or *SOX9*.EC3 sgRNA [Kolmogorov-Smirnov (KS) test, *n* = cells]. Mean (±SD) perimeters (micrometers): (C) Left: CTRL/*SOX9*.EC1 sgRNA: 3.78 (±2.63)/4.36 (±2.63); middle: CTRL/*SOX9*.EC2 sgRNA: 3.78 (±2.63)/4.47 (±2.64); right: CTRL/*SOX9*.EC3 sgRNA: 3.39 (±2.56)/4.28 (±2.65). (G) Left: CTRL/*SOX9*.EC1 sgRNA: 3.83 (±2.71)/4.45 (±2.72); middle: CTRL/*SOX9*.EC2 sgRNA: 3.19 (±2.44)/4.26 (±2.61); right: CTRL/*SOX9*.EC3 sgRNA: 3.83 (±2.71)/4.22 (±2.56). (**D** and **G**) Allele percentages with *SOX9* promoter interacting with *SOX9*.EC1, *SOX9*.EC3, or both (D) and *SOX9*.EC1, *SOX9*.EC3, or both (G) in MB157–dCas9-KRAB expressing CTRL, *SOX9*.EC1, *SOX9*.EC2, or *SOX9*.EC3 sgRNA (*n* = alleles). (**E** and **H**) Representative cells of 3C and 3D (E) or 3F and 3G (H). Blue: DAPI. (**I**) *SOX9* promoter inactivation decreases *SOX9*-EC1-EC3 three-way interaction frequency across individual alleles in TNBC MB157. Top-left: Allele percentages with *SOX9* promoter interacting with *SOX9*.EC1, *SOX9*.EC3, or both in MB157–dCas9-KRAB expressing CTRL or *SOX9* promoter sgRNA (*SOX9*.P sgRNA) (*n* = alleles). Bottom-left: CDFs of *SOX9*-EC1-EC3 spatial perimeter in each MB157–dCas9-KRAB cell (KS test, *n* = cells). CTRL/*SOX9*.P sgRNA mean (±SD) perimeter: 3.90 (±2.62)/4.44 (±2.66) μm. Right: Representative cells. Blue: DAPI. Scale bars, 3 μm for nuclei and 0.5 μm for alleles.

and transcriptional coactivator mastermind like transcriptional co-activator 1 (MAML1)—showed that NTCs bind the *SOX9* promoter, *SOX9*.EC1, *SOX9*.EC2, and *SOX9*.EC3 enhancer clusters (Fig. 4A). Inhibition of Notch signaling by gamma secretase inhibitor (GSI) (Fig. 4, A and B) led to significant and concomitant loss of NICD1 (fig. S4A), down-regulation of Notch canonical targets (fig. S4B), decreased proliferation (fig. S4C), reduction in *SOX9* levels (fig. S4A), and almost completely abolished NTC binding to *SOX9* enhancer clusters (Fig. 4A). Notably, genome-wide examination of Notch-dependent loops within hyper-interacting hubs showed that Notch binds to 6.5% of genomic elements at both ends of the Notch-dependent loops, including *SOX9* (fig. S4D). In sum, these data suggest that Notch signaling is required for binding of NTC to *SOX9* enhancer clusters and *SOX9* expression.

To investigate whether NTC chromatin binding positions *SOX9* enhancers within individual TNBC nuclei, we mapped the 3D distance between the *SOX9* promoter and *SOX9*.EC1, *SOX9*.EC2, and *SOX9*.EC3 before and after GSI treatment. Reproducibly, loss of NTC chromatin binding significantly separated the *SOX9* promoter from all three enhancers (Fig. 4, C to E, and fig. S4, E to G). By contrast, loss of NTC chromatin binding did not increase the distance between the *SOX9* promoter and a control probe (fig. S4H) located outside of the *SOX9* promoter-enhancer hub (Fig. 4A). Evaluation of pairwise interaction frequencies between the *SOX9* promoter and its three enhancer clusters in individual TNBC MB157 cells supported these data and further revealed that loss of NTC chromatin binding resulted in 13.8, 9.8, and 10.0% fewer MB157 cells with *SOX9* promoter to *SOX9*.EC1, *SOX9*.EC2, and *SOX9*.EC3 interactions, respectively (fig. S4I). Thus, our observations suggest that NTC binding to *SOX9* enhancer clusters decreases *SOX9* promoter-enhancer proximity and promotes *SOX9* expression.

Notch transcription complex chromatin binding compacts *SOX9* promoter-enhancer hubs

Given that loss of NTC chromatin binding separated the *SOX9* promoter from each of its enhancer clusters, we next investigated whether NTC chromatin binding contributes to compaction of *SOX9* promoter-enhancer hubs. To this end, we measured the spatial perimeters of *SOX9*-EC1-EC3 and *SOX9*-EC2-EC3 hubs in individual TNBC MB157 cells after Notch inhibition. We reproducibly observed that loss of NTC chromatin binding significantly increased spatial perimeters of *SOX9* promoter and its enhancer clusters (Fig. 4, F and G, and fig. S4, J and K). Concordantly, we observed decreases in multiway interaction frequencies between the *SOX9* promoter and its enhancer clusters across individual alleles. In the absence of NTC chromatin binding, the number of alleles in which the *SOX9* promoter interacted with none of the *SOX9* enhancer clusters increased by 38.5 and 18.4% in *SOX9*-EC1-EC3 and *SOX9*-EC2-EC3 hubs, respectively (Fig. 4, F and G). On the other hand, we observed minimal multiway interactions between the *SOX9* promoter, the control probe located outside the *SOX9* hub region, and *SOX9*.EC1 or *SOX9*.EC2 (fig. S4, L and M), indicating that NTC chromatin binding only affects spatial positioning of the *SOX9* promoter and enhancer clusters and not the genomic elements outside the *SOX9* spatial hub. As an additional control, we measured interactions between the promoter of *IKZF2*, a hematopoietic-specific transcription factor inactive in breast cancer cells, and its 5′ and 3′ TAD boundaries in MB157 treated with dimethyl sulfoxide (DMSO) or GSI. Single-allele analysis showed that multiway interactions

between the *IKZF2* promoter and its TAD boundaries were invariant, indicating that the regulation of chromatin topology by NTC is not ubiquitous and is restricted to its target genes (fig. S4N). Taken in conjunction, our data suggest that NTC recruitment to chromatin contributes to the regulation of *SOX9* promoter-enhancer hub topology by increasing multiway interactions between the *SOX9* promoter and its three distal enhancer clusters.

Notch transcription complex activity is required for the positioning and compaction of *SOX9* promoter-enhancer hubs

Intrigued by the observation that NTC chromatin binding is required for multiway interactions at the *SOX9* locus (Fig. 4, F and G, and fig. S4, J and K), we aimed to elucidate the role of NTC activity in addition to its chromatin binding in *SOX9* promoter-enhancer hub formation. To this end, we generated a doxycycline (DOX)–inducible green fluorescent protein (GFP)–fused dominant negative form of MAML1 (dnMAML) (Fig. 5A and fig. S5A). In line with earlier studies showing that dnMAML forms transcriptionally inert ternary NTC without abrogating its chromatin binding ability (*47*), we observed that dnMAML induction markedly down-regulated canonical Notch targets (fig. S5B), impaired proliferation (fig. S5C), and, similar to NTC chromatin binding loss, reduced SOX9 without affecting NICD1 levels (fig. S5D) in MB157 cells.

To examine the requirement of NTC activity for *SOX9* promoter-enhancer interactions, we measured the 3D distance of *SOX9* promoter to *SOX9*.EC1, *SOX9*.EC2, and *SOX9*.EC3 enhancer clusters in individual dnMAML-expressing MB157 cells. DnMAML-mediated NTC inactivation reduced the number of cells with pairwise interactions between the *SOX9* promoter and *SOX9*.EC1, *SOX9*.EC2, and *SOX9*.EC3 by 23.0, 35.4, and 48.6%, respectively (fig. S5E). Concordantly, distances between the *SOX9* promoter and all three enhancer clusters significantly and reproducibly increased (Fig. 5, B to D, and fig. S5, F to H). By contrast, NTC inactivation did not significantly change the distance between the *SOX9* promoter and the control probe marking a genomic element outside the *SOX9* promoter-enhancer hub (fig. S5I and Fig. 4A). Thus, NTC chromatin binding is not sufficient, and its activity is required for the spatial positioning of the *SOX9* promoter and enhancer clusters in individual TNBC nuclei.

To test whether NTC activity is required for multiway interactions and compaction of *SOX9* promoter-enhancer hubs, we compared *SOX9*-EC1-EC3 and *SOX9*-EC2-EC3 multiway interactions and spatial hub compaction in individual MB157 cells before and after dnMAML induction. In line with GSI treatment abrogating NTC chromatin binding, dnMAML-mediated NTC inactivation markedly and reproducibly increased the spatial perimeters of *SOX9*-EC1-EC3 and *SOX9*-EC2-EC3 promoter-enhancer hubs (Fig. 5, E and F, and fig. S5, J and K). Concordantly, examination of multiway interactions in individual alleles revealed that the frequency of three-way interactions involving *SOX9*, *SOX9*.EC1, and *SOX9*.EC3 as well as *SOX9*, *SOX9*.EC2, and *SOX9*.EC3 was reduced by up to 50.8 and 41.4%, respectively (Fig. 5, E and F). In the absence of NTC activity, the *SOX9* promoter did not interact with either of the probed enhancer clusters in ~60% of alleles. On the other hand, NTC inactivation had minimal effect on multiway interactions between the *SOX9* promoter, *SOX9*.EC1, and the control probe located outside the *SOX9* spatial hub region (fig. S5L and Fig. 4A), indicating that NTC activity specifically affects spatial positioning of the
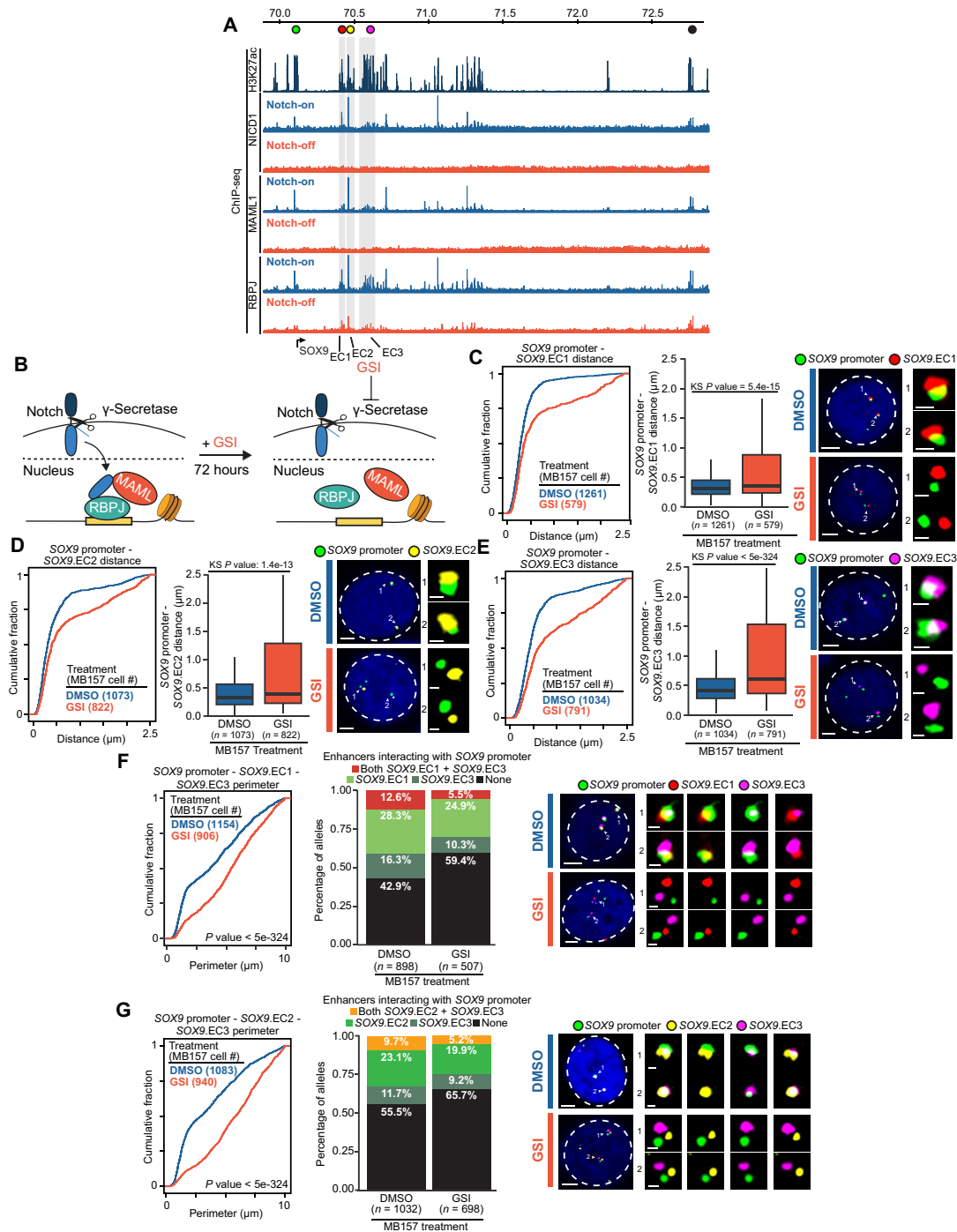
Fig. 4. Notch transcription complex (NTC) chromatin binding compacts *SOX9* promoter-enhancer hubs. (**A**) GSI-mediated Notch signaling inhibition abrogates NTC binding to *SOX9* enhancers. Genome tracks from top to bottom: Circles marking location of Oligopaint probes labeling the *SOX9* promoter (green), *SOX9*.EC1 (red), *SOX9*.EC2 (yellow), *SOX9*.EC3 (magenta), and control (black) and H3K27ac, Notch intracellular domain (NICD1), MAML1, and RBPJ ChIP-seq before (blue) and after (orange) GSI treatment in MB157. (**B**) GSI inhibits the cleavage of NICD1 (light blue) from extracellular domain (dark blue), preventing ternary NTC complex formation on chromatin. (**C** to **E**) NTC chromatin binding loss separates *SOX9* promoter from *SOX9*.EC1 (C), *SOX9*.EC2 (D), or *SOX9*.EC3 (E). CDFs (left) and box and whiskers (middle) of *SOX9* promoter and *SOX9*.EC1 (C), *SOX9*.EC2 (D), and *SOX9*.EC3 (E) distances in dimethyl sulfoxide (DMSO)– or GSI-treated MB157 (KS test, *n* = cells). DMSO/GSI mean (±SD) distance between *SOX9* promoter and *SOX9*.EC1 (C): 0.394 (±0.333)/0.707 (±0.708) μm; *SOX9*.EC2 (D): 0.516 (±0.536)/0.765 (±0.735) μm; *SOX9*.EC3 (E): 0.574 (±0.495)/0.946 (±0.725) μm. Right: Representative cells. Scale bars are similar to those observed in Fig. 3A Blue: DAPI. (**F** and **G**) NTC chromatin binding loss decompacts and decreases three-way interactions in *SOX9*-EC1-EC3 (F) and *SOX9*-EC2-EC3 (G) hubs. Left: CDFs of *SOX9*-EC1-EC3 (F) and *SOX9*-EC2-EC3 (G) spatial perimeters in DMSO- or GSI-treated MB157 (KS test, *n* = cells). DMSO/GSI mean (±SD) perimeter *SOX9*-EC1-EC3 (F): 3.94 (±2.75)/5.31 (±2.61) μm; *SOX9*-EC2-EC3 (G): 3.66 (±2.65)/5.65 (±2.59) μm. Middle: Bar plot of percentage of alleles with *SOX9* promoter interacting (<350 nm) with *SOX9*.EC1, *SOX9*.EC3, or both (F) and with *SOX9*.EC2, *SOX9*.EC3, or both (G) (*n* = alleles). Right: Representative cells. Scale bar per 3A. Blue: DAPI.
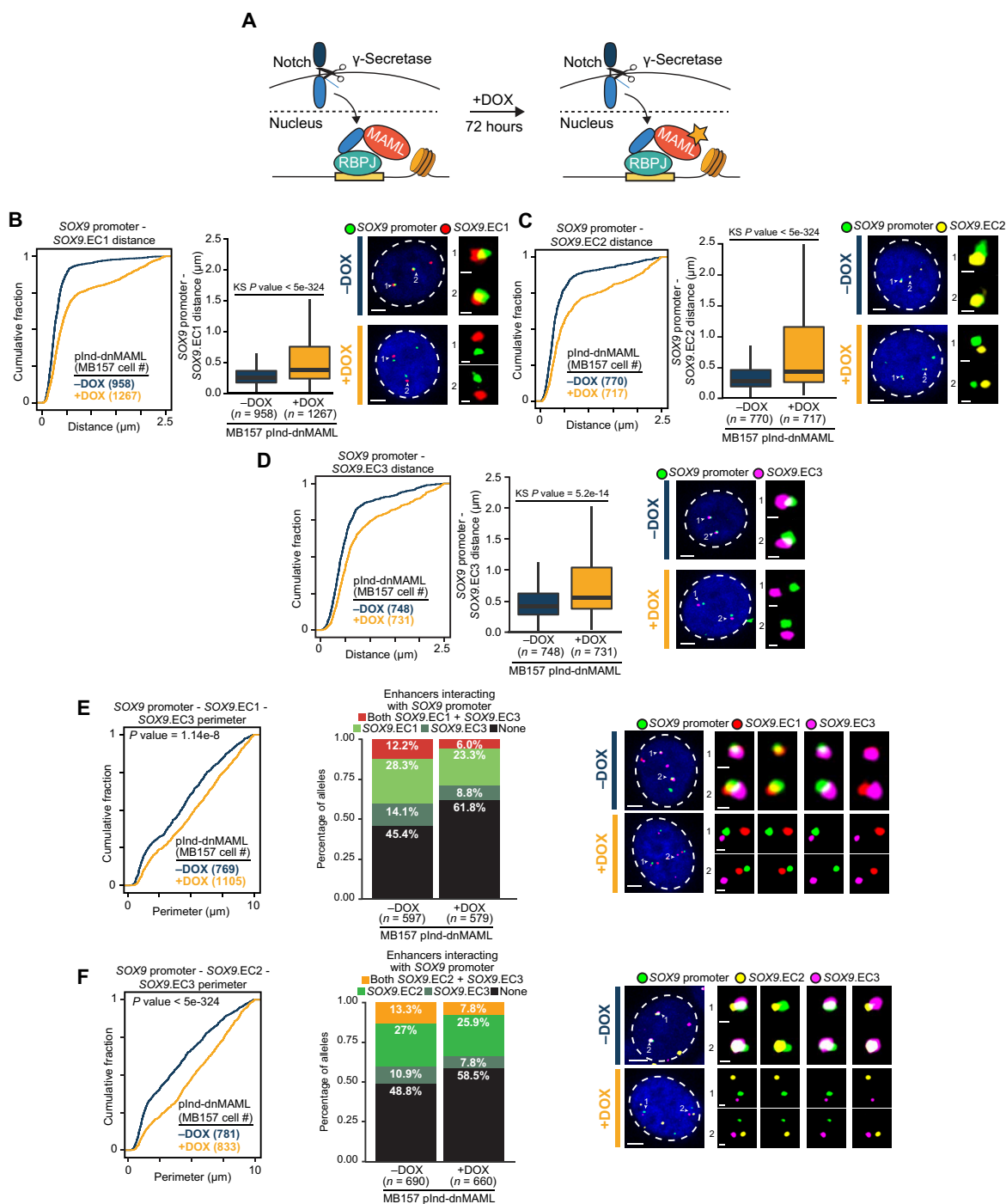
Fig. 5. NTC activity is required for positioning and compaction of *SOX9* promoter-enhancer hubs. (**A**) Schematic showing expression of dnMAML after 72-hour DOX treatment, which competitively binds to NICD1 (light blue) and RBPJ (teal) to form an inactive ternary NTC. (**B** to **D**) NTC inactivation significantly increases 3D distances between *SOX9* promoter and *SOX9*.EC1 (B), *SOX9*.EC2 (C), or *SOX9*.EC3 (D) in individual MB157. CDFs (left) and box and whiskers (middle) of *SOX9* promoter and *SOX9*.EC1 (B), *SOX9*.EC2 (C), and *SOX9*.EC3 (D) distances in each pInd-dnMAML–expressing MB157 (MB157-pInd-dnMAML) without DOX (−DOX) or with DOX (+DOX) treatment (KS test, *n* = cells). Probe locations per 4A. −DOX/+DOX mean (±SD) distance between *SOX9* promoter and *SOX9*.EC1 (B): 0.336 (±0.325)/0.671 (±0.655) μm; *SOX9*.EC2 (C): 0.451 (±0.490)/0.777 (±0.723) μm; *SOX9*.EC3 (D): 0.561 (±0.469)/0.815 (±0.638) μm. Right: Representative cells. Scale bar per 3A. Blue: DAPI. (**E** and **F**) NTC inactivation expands *SOX9*-EC1-EC3 (E) and *SOX9*-EC2-EC3 (F) promoter-enhancer hubs in individual MB157 and decrease three-way interaction frequency across individual alleles. Left: CDFs of *SOX9*-EC1-EC3 (E) and *SOX9*-EC2-EC3 (F) spatial perimeters in each −DOX and +DOX MB157-pInd-dnMAML cell (KS test, *n* = cells). −DOX/+DOX mean perimeter (±SD): *SOX9*-EC1-EC3: 4.33 (±2.68)/5.21 (±2.78) μm; *SOX9*-EC2-EC3: 3.90 (±2.71)/5.2 (±2.75) μm. Middle: Bar plots of allele percentages with *SOX9* promoter interacting (<350 nm) with *SOX9*.EC1, *SOX9*.EC3, or both (E) and *SOX9*.EC2, *SOX9*.EC3, or both (F) in −DOX and +DOX MB157-pInd-dnMAML (*n* = alleles). Right: Representative cells. Scale bar per 3A. Blue: DAPI.

SOX9 promoter and enhancer clusters within the *SOX9* spatial hub and not the genomic elements outside it. Together, our single-cell/allele data show that NTC activity, and not just its assembly on chromatin, is required for positioning of the *SOX9* regulatory elements and compaction of *SOX9* promoter-enhancer hubs in individual TNBC cells.

Transcription inhibition expands *SOX9* promoter-enhancer hubs

Intrigued by our observation that NTC activity was required for *SOX9* promoter-enhancer hub compaction, we aimed to investigate whether this effect arises from potential synergistic interactions with the transcriptional machinery. To this end, we inhibited transcription initiation and elongation in MB157 by treating cells with triptolide and THZ1 for 5 hours, respectively. Triptolide is now in phase 1 clinical trial for treatment of advanced solid breast tumors (ClinicalTrials.gov identifier: NCT03129139), and THZ1 has shown efficacy in treating TNBC tumors (*48*). Triptolide treatment reduced *SOX9* expression by 96% and *SOX9*-EC1-EC3 three-way interactions by 42.8% in individual alleles (fig. S5, M and N). These results are in line with a recent Micro-C study showing that triptolide treatment weakens enhancer-promoter (EP) interactions across a cell population (*49*). In comparison, inhibiting transcription elongation with THZ1 (*50*) led to a smaller reduction in *SOX9* expression but had a stronger effect on *SOX9* hub topology, decreasing multiway interactions by 58.6% (fig. S5, M and N). In contrast, interactions between the *IKZF2* promoter and its 5′ and 3′ TAD boundaries remained relatively stable after triptolide and THZ1 treatments, as the percentage of alleles in which the *IKZF2* promoter interacted with neither TAD boundary increased by <10% (fig. S5O). Together, these data suggest that while neither treatment completely abrogated promoter-enhancer interactions at the *SOX9* locus, transcriptional activity promotes the compaction of *SOX9* spatial hubs.
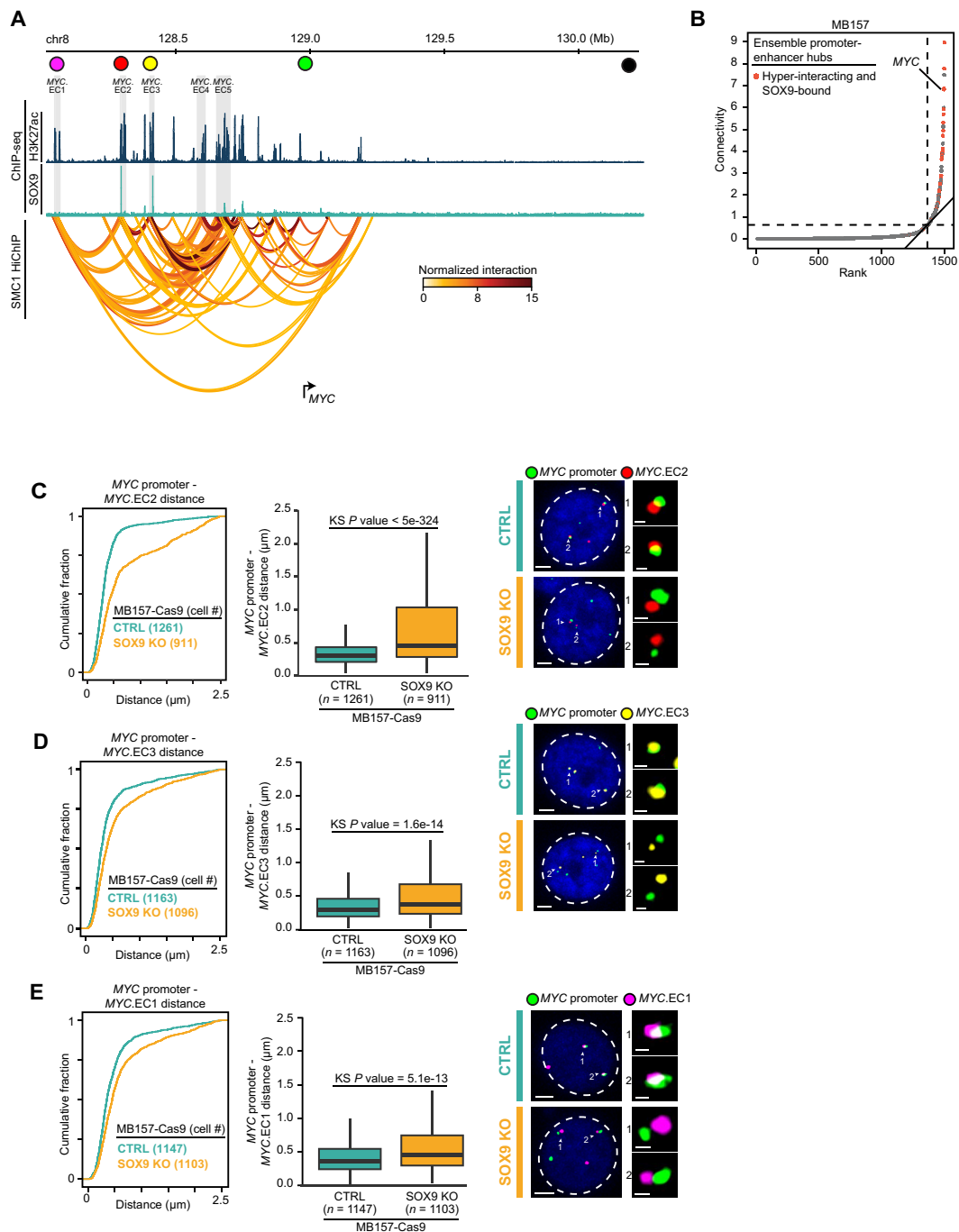
SOX9 regulates oncogene *MYC* by positioning its enhancers

Intrigued by the observation that signaling-dependent Notch transcription factor promotes multiway interactions and promoter-enhancer hub compaction (Figs. 4, F and G, and 5, E and F), we sought to investigate whether lineage-determining transcription factors similarly promote formation of promoter-enhancer hubs in individual TNBC cells. Lineage-determining transcription factor SOX9 is a proliferation (Fig. 1, B and C) and stem cell factor in breast cancer (*21*, *27*, *51*). Integrated transcriptomics, H3K27ac chromatin immunoprecipitation sequencing (ChIP-seq), and SOX9 chromatin binding analysis in TNBC MB157 revealed that SOX9 promotes expression of 952 genes [false discovery rate (FDR) < 0.01, log$_2$ fold change (FC) < −0.5] (fig. S6A and table S2), which are predominantly involved in pathways promoting ER$^-$ breast cancer pathogenesis, including *MYC* target genes (fig. S6B). Integration of these results with SMC1 HiChIP data further revealed that population-based hyper-interacting hubs exhibit higher SOX9 binding to pairs of interacting promoters and/or enhancers compared to nonhyper-interacting hubs (fig. S6C). Notably, 80% (56 of 70) of significantly down-regulated genes with SOX9-bound promoter and distal enhancer, including *MYC*, participate in population-based hyper-interacting promoter-enhancer hubs (Fig. 6, A and B, and table S3).

Given that loss of SOX9 significantly down-regulated MYC target genes (fig. S6B), we closely examined the regulatory relationship between SOX9 and MYC. Genomic deletion of SOX9 markedly down-regulated *MYC* expression in MB157 cells (log$_2$ FC = −0.91, FDR = 1.44×10^{-139}) (fig. S6A). Close inspection of the *MYC* locus revealed that it was differentially acetylated in TNBC and ER$^+$ breast cancer (fig. S6D). In TNBC MB157 and MDA-MB-468, the region 5′ of the *MYC* promoter was highly acetylated. By contrast, this region was epigenetically inactive in ER$^+$ MCF7. Integration of H3K27ac and SOX9 ChIP-seq data further showed that two of the five highly acetylated genomic elements located 436 kb and 330 kb 5′ of the *MYC* promoter, referred to as *MYC*.EC2 and *MYC*.EC3, bind SOX9 in TNBC cells and highly interact with the *MYC* promoter (Fig. 6A and fig. S6, D and E). H3K27ac Cut&Run analysis further showed that loss of SOX9 markedly reduces H3K27ac at these genomic elements, indicating that SOX9 may regulate *MYC* through activating elements within these putative enhancer clusters (fig. S6F). To substantiate the potential subtype-restricted regulatory relationship between MYC and SOX9, we evaluated *MYC* expression levels 3 days after SOX9 genomic deletion in TNBC MB157 and MDA-MB-468 as well as ER$^+$ MCF7 cells. This analysis showed that loss of SOX9 significantly down-regulates *MYC* transcript and MYC protein levels in TNBC but not ER$^+$ cells (fig. S6, G and H). Furthermore, dCas9-KRAB–mediated inactivation of genomic elements within *SOX9*.EC1 and *SOX9*.EC3 in four biological replicates showed that loss of *SOX9* enhancer activity down-regulates *MYC* expression in TNBC MDA-MB-468 and MB157 but not non-TNBC MCF7 (fig. S6I). Our data showed that targeting *SOX9*.EC2 also reduces *MYC* expression, albeit at a lesser extent due to variability in response across our four biological replicates. Collectively, these data suggest that SOX9 and its enhancers can fine-tune *MYC* expression. Concordantly, *MYC* and *SOX9* expression levels were positively correlated in primary ER$^-$ but not ER$^+$ tumors (fig. S6J). Together, these results suggest that SOX9 can regulate *MYC* expression potentially through subtype-restricted enhancers.

To determine whether SOX9 can influence *MYC* enhancer positioning in a subtype-restricted manner, we optically mapped the 3D distance between the *MYC* promoter and its two SOX9-bound enhancer clusters, *MYC*.EC2 and *MYC*.EC3, after genomic deletion of *SOX9* in individual TNBC and ER$^+$ breast cancer cells. Examination of more than 900 cells per condition in TNBC MB157 revealed that loss of SOX9 significantly and reproducibly separates the *MYC* promoter from its two SOX9-bound enhancers, with the mean promoter-enhancer distance increasing by 360 and 144 nm for *MYC*.EC2 and *MYC*.EC3, respectively (Fig. 6, C and D, and fig. S6, K and L). Concordantly, we observed separation of the *MYC* promoter from *MYC*.EC3 in SOX9-deficient MDA-MB-468 after optically mapping the distance between these two regulatory elements in more than 2000 SOX9 proficient and deficient cells (fig. S6M). By contrast, loss of SOX9 did not significantly separate the *MYC* promoter from the *MYC*.EC3 genomic element in ER$^+$ MCF7 (fig. S6N), where *MYC* expression was SOX9 independent (fig. S6, G and H). As an additional control, we measured the distance between the *MYC* promoter and a 3′ *MYC* genomic element that functions as a T cell lymphoblastic leukemia (T-ALL)–specific *MYC* enhancer (Fig. 6A) (*18*, *52*). Unlike TNBC *MYC*.EC2 and *MYC*.EC3 enhancer clusters, the distance between the control probe marking the T-ALL-specific enhancer and the *MYC* promoter did not significantly increase after SOX9 deletion in TNBC MB157 (fig. S6O). In line with these data, SOX9 loss decreased the number of cells with *MYC* to *MYC*.EC2 and *MYC* to *MYC*.EC3 interacting alleles by 41.1 and 23.8%, respectively (fig. S6P). By contrast, *SOX9* deletion did not decrease the

Fig. 6. SOX9 regulates oncogene *MYC* by positioning its enhancers. (**A**) Genome tracks showing enrichment of pairwise *MYC* enhancer-enhancer and promoter-enhancer interactions in a population of MB157 cells. From top to bottom: Colored circles marking location of Oligopaint DNA FISH probes labeling 50-kb regions at *MYC* promoter (green), *MYC*.EC1 (magenta), *MYC*.EC2 (red), *MYC*.EC3 (yellow), and T-ALL–restricted enhancer (black), H3K27ac and SOX9 levels as measured by ChIP-seq, and normalized interaction frequency as measured by SMC1 HiChIP at the *MYC* locus in MB157. *MYC* enhancer clusters are marked by grey boxes. (**B**) A total of 80% of differentially expressed genes with SOX9-bound promoter and distal enhancer participate in ensemble hyper-interacting hubs. MB157 hubs plotted in ascending order of their total connectivity as measured by SMC1 HiChIP in TNBC MB157. Hyper-interacting promoter-enhancer hubs are defined as the ones above the elbow of the ranked total connectivity plot. Hyper-interacting ensemble promoter-enhancer hubs containing genes that are significantly down-regulated in MB157-Cas9 cells transfected with SOX9 targeting sgRNA versus control sgRNA for 4 days and have SOX9-bound promoter and distal enhancer are marked in orange. (**C** to **E**) SOX9 loss significantly increases 3D distances between the *MYC* promoter and SOX9-bound *MYC*.EC2 (C) or *MYC*.EC3 (D) and SOX9-unbound *MYC*.EC1 (E) in individual cells. CDFs (left) and box and whiskers (middle) of the distances between the *MYC* promoter and SOX9-bound *MYC*.EC2 (C) and *MYC*.EC3 (D) and SOX9-unbound *MYC*.EC1 (E) in each MB157-Cas9 6 days after transduction with control sgRNA (CTRL) or SOX9-targeting sgRNA (SOX9 KO) (KS test, *n* = cells). Probe locations per 6A. CTRL/SOX9 KO mean (±SD) distance between *MYC* promoter and *MYC*.EC2: 0.389 (±0.358)/0.749 (±0.666) μm; *MYC*.EC3: 0.447 (±0.457)/0.591 (±0.551) μm; *MYC*.EC1: 0.494 (±0.447)/0.651 (±0.556) μm. Right: Representative cells. Scale bar per 3A. Blue: DAPI.

number of cells with *MYC* to control probe interacting alleles (fig. S6P). In sum, these observations indicate that SOX9 regulates *MYC* expression by promoting proximity between the *MYC* promoter and subtype-restricted SOX9-bound enhancers in TNBC.

Given the observation that the activity of one enhancer contributes to the positioning of another enhancer within the *SOX9* promoter-enhancer hub (Fig. 3, C to H), we examined how loss of SOX9 at *MYC*.EC2 and *MYC*.EC3 affects the positioning of the *MYC* promoter and SOX9-unbound *MYC*.EC1 enhancer, located 679 kb upstream of the *MYC* promoter. Loss of SOX9 significantly increased the distance between the *MYC* promoter and *MYC*.EC1 in TNBC MB157 and MDA-MB-468 but not in ER⁺ MCF7 (Fig. 6E and fig. S6, Q, R, and S). In tandem with the impact of SOX9 on *MYC* promoter-enhancer distances, we observed that loss of SOX9 decreased the number of cells with a *MYC* to *MYC*.EC1 interacting allele by 27.3% (fig. S6P). The observation that loss of SOX9 repositioned both SOX9-bound and SOX9-unbound enhancers at the *MYC* locus indicates that *MYC* enhancers may cooperate, allowing SOX9 to compact the *MYC* promoter-enhancer hub, paralleling the effect of NTC on these topological assemblies at the *SOX9* locus. These data also suggest that SOX9 promotes the expression of its target genes by facilitating promoter-enhancer interactions, a previously unrecognized capability of this lineage-determining transcription factor.

SOX9 loss decompacts *MYC* promoter-enhancer hubs
Given that loss of SOX9 separates the *MYC* promoter from its interacting enhancers, we next investigated whether pairwise interacting *MYC* promoter and distal enhancer clusters are engaged in multiway interactions and form promoter-enhancer hubs in individual TNBC cells. To this end, we first measured the 3D distance between the *MYC* promoter, SOX9-bound *MYC*.EC3, and SOX9-unbound *MYC*.EC1 and examined the frequency of pairwise and multiway interactions among them in individual alleles. Analysis of >1300 alleles in each of the MB157, MDA-MB-468, and MCF7 revealed that the frequency of alleles with multiway interactions among the *MYC* promoter and *MYC*.EC1 and *MYC*.EC3 enhancer clusters (referred to as *MYC*-EC1-EC3 hub) was 16.4 and 19.9% in MB157 and MDA-MB-468, respectively, but was only 3.8% in ER⁺ MCF7 cells (Fig. 7A). In more than 60.0% of alleles, the *MYC* promoter interacted with *MYC*.EC1, *MYC*.EC3, or both *MYC*.EC1 and *MYC*.EC3 (Fig. 7A). By contrast, ~70% of the *MYC* promoters in ER⁺ MCF7 breast cancer cells did not interact with either *MYC*.EC1 or *MYC*.EC3.

After establishing that the *MYC* promoter and its enhancer clusters form a TNBC-restricted promoter-enhancer hub at single-allele resolution, we next examined the SOX9 dependency of these topological assemblies by calculating the spatial perimeter between the *MYC* promoter, SOX9-unbound *MYC*.EC1, and SOX9-bound *MYC*.EC2 (referred to as *MYC*-EC1-EC2 hub) before and after *SOX9* deletion in individual cells. Loss of SOX9 markedly increased the perimeters of the *MYC*-EC1-EC2 hubs (Fig. 7B). Concomitant with the expansion of the *MYC*-EC1-EC2 hubs, SOX9 loss reproducibly reduced the frequency of alleles with *MYC*-EC1-EC2 three-way interactions by up to 43.0%, with 67.0% of *MYC* promoters not interacting with either regulatory element (Fig. 7B and fig. S7A). Similarly, examination of the *MYC* promoter, *MYC*.EC1, and *MYC*.EC3 spatial perimeters and three-way interactions showed that SOX9 loss expanded *MYC* promoter-enhancer hubs (Fig. 7C) and reproducibly decreased three-way *MYC*-EC1-EC3 interaction frequency by up to

42.0 and 45.7% in MB157 and MDA-MB-468 cells, respectively (Fig. 7C and fig. S7, B and C). By contrast, loss of SOX9 did not change the frequency of *MYC*-EC1-EC3 three-way interactions in ER⁺ MCF7 (fig. S7D), where *MYC* expression was SOX9 independent (fig. S6, G and H). Similarly, three-way interaction frequencies among the control probe marking the T-ALL-specific enhancer, the *MYC* promoter, and *MYC*.EC2 (fig. S7E) or *MYC*.EC3 enhancer clusters (fig. S7F) were markedly lower than *MYC*-EC1-EC2 and *MYC*-EC1-EC3 interactions and were unaffected by SOX9 loss.

In tandem with our results on the impact of Notch on the *SOX9* promoter-enhancer hub, our data from the *MYC* locus studies further corroborate the role of promoter-enhancer hubs in facilitating cross-stabilization of enhancers, as the absence of SOX9 decompacted the *MYC* spatial hub and even repositioned a SOX9-unbound enhancer. In summary, our findings demonstrate that in addition to facilitating promoter-enhancer looping, SOX9 is able to regulate its target genes in TNBC by promoting multiway interactions between distal enhancers and a gene promoter.

Notch promotes compaction of *MYC* promoter-enhancer hubs
Earlier studies have shown the ability of Notch in promoting pairwise interactions between the *MYC* promoter and its enhancers (*6*). Here, our data showed that activity of NTC compacts *SOX9* promoter-enhancer hubs (Fig. 4, F and G, and fig. S4, J and K). We thus investigated whether this signaling-dependent transcription factor can also regulate the spatial hub assembly at the *MYC* locus. To this end, we first examined whether SOX9 and Notch can cooperate to regulate *MYC*. GSI-mediated inhibition of Notch signaling with or without SOX9 genomic deletion showed that loss of SOX9 further reduces *MYC* expression by an additional 37.4% compared to GSI treatment alone, suggesting potential cooperation between the two transcription factors in regulating *MYC* (fig. S7G).

Examination of *MYC* promoter-enhancer hubs further showed that Notch inactivation results in a 35.6% reduction in three-way interactions between the *MYC* promoter, *MYC*.EC1, and *MYC*.EC3 (fig. S7H) and a 59.4% reduction in three-way interactions between the *MYC* promoter, *MYC*.EC2, and *MYC*.EC4 (fig. S7I). Together, these data indicate that in addition to SOX9, Notch activity also promotes *MYC* spatial hub compaction, further supporting the role of oncogenic transcription factors in aberrant promoter-enhancer hub formation in TNBC.

DISCUSSION
Spatial promoter-enhancer hub has emerged as a unit of chromatin organization with enigmatic topological structure and biological relevance in cancer. In this study, we aimed to elucidate the organizational principles, regulators, and functions of promoter-enhancer hubs by examining the topology of TNBC genome at single-cell resolution. Through optical mapping of promoter-enhancer interactions, we dissected TNBC-restricted promoter-enhancer hubs at the *SOX9* and *MYC* loci—two regions residing among the most hyper-interacting spatial hubs in the TNBC genome. Our single-cell/single-allele investigations revealed that multiway interactions between the gene promoter and multiple TNBC-restricted enhancer clusters occur in individual cancer cells, and the frequency of these interactions is positively associated with gene expression, observations that may extend to other loci.
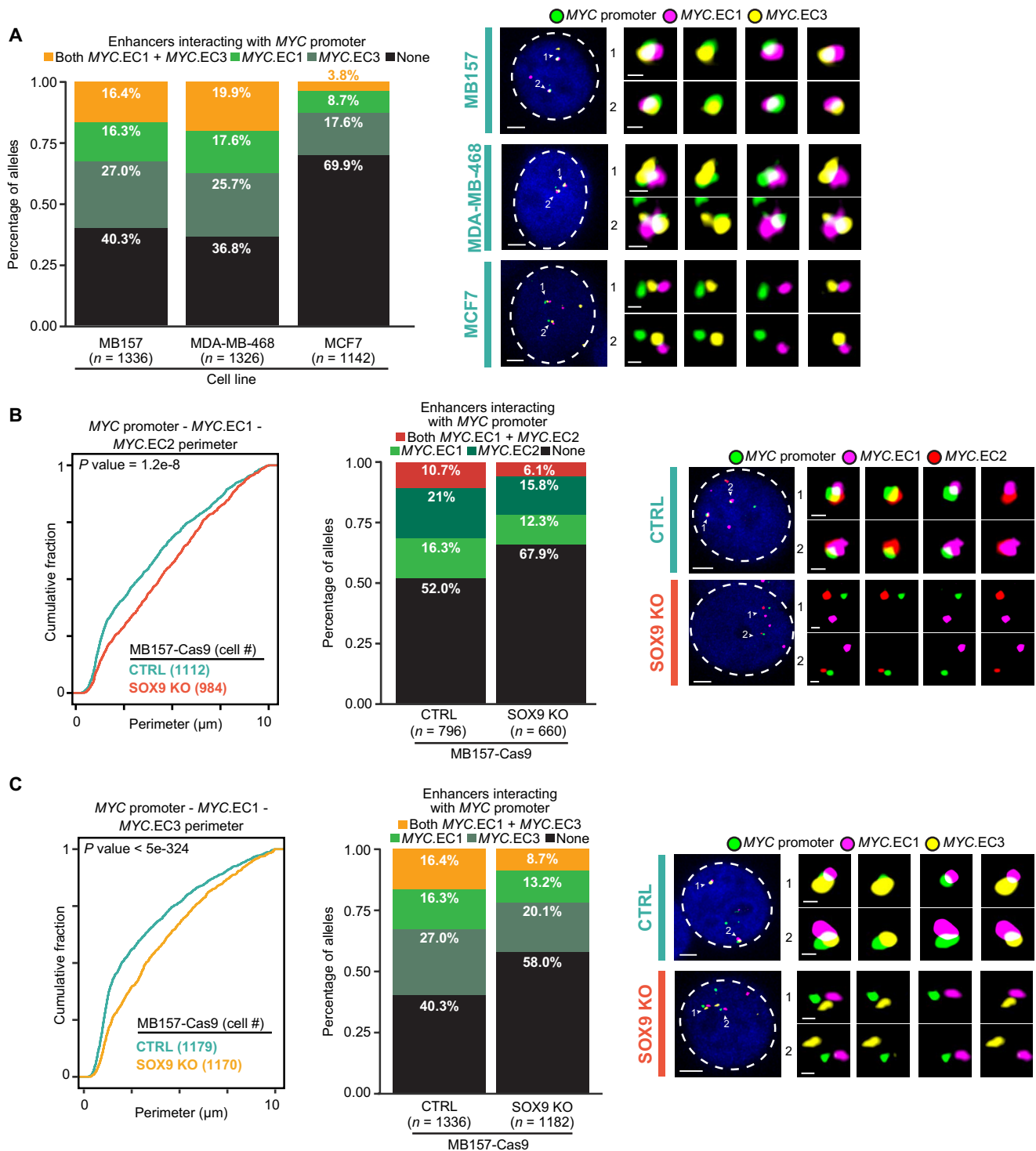
Fig. 7. SOX9 loss decompacts *MYC* promoter-enhancer hubs. (**A**) *MYC* promoter participates in multiway interactions with its distal enhancer clusters in individual TNBC MB157 and MDA-MB-468 but not ER⁺ MCF7. Left: Percentage of alleles with *MYC* promoter interacting (<350 nm) with SOX9-unbound *MYC*.EC1, SOX9-bound *MYC*.EC3, or both *MYC*.EC1 and *MYC*.EC3 in MB157, MDA-MB-468, and MCF7 as measured by three-color Oligopaint DNA FISH with probes marked in Fig. 6A top genome track (*n* = alleles). Right: Representative MB157, MDA-MB-468, and MCF7 nuclei and two magnified alleles from three-color DNA FISH. Scale bar per 3A. Blue: DAPI. (**B** and **C**) SOX9 loss expands *MYC*-EC1-EC2 (B) and *MYC*-EC1-EC3 (C) promoter-enhancer hubs in individual MB157 and decreases three-way interaction frequency across individual alleles. Left: CDFs of *MYC*-EC1-EC2 (B) and *MYC*-EC1-EC3 (C) spatial perimeters in each MB157-Cas9 cell expressing CTRL or SOX9 KO sgRNA (KS test, *n* = cells). Probe locations per 6A. CTRL/SOX9 KO mean (±SD) perimeters *MYC*-EC1-EC2 (B): 3.84 (±2.70)/4.53 (±2.67) µm; *MYC*-EC1-EC3 (C): 3.10 (±2.58)/3.90 (±2.64) µm (*n* = cells). Middle: Allele percentages with *MYC* promoter interacting (<350 nm) with *MYC*.EC1, *MYC*.EC2, or both *MYC*.EC1 and *MYC*.EC2 (B) and *MYC*.EC1, *MYC*.EC3, or both *MYC*.EC1 and *MYC*.EC3 (C) in CTRL and SOX9 KO MB157-Cas9. Right: Representative cells. Scale bar per 3A. Blue: DAPI.

Furthermore, our findings provide additional evidence supporting the crucial role of transcription factors in regulating promoter-enhancer hubs (*4*, *53*), as demonstrated by data showing the decompaction of *SOX9* and *MYC* spatial hubs in individual cells following the loss of NTC and SOX9 chromatin binding, respectively. Specifically, the inability of inert chromatin-bound NTC and inhibited transcription in compacting *SOX9* spatial hubs underscores the requirement for the complex's activity and potential involvement of coactivators as well as active transcription in spatial hub formation. Although a comparison with the TNBC cell of origin is necessary, the observation that lineage-determining and signaling-dependent transcription factors, crucial in ER⁻ luminal stem/progenitor cells, can determine promoter-enhancer hub compaction in TNBC suggests an additional mechanism by which dysregulated transcription factors can establish oncogenic transcriptional programs during tumor initiation and progression. This observation aligns with evidence from ensemble hubs in other cancer types, reinforcing the broader implications of our findings (*7*, *17*).

We additionally found that enhancer activity also increases promoter-enhancer hub compaction. We found that inactivation of individual *SOX9* enhancers resulted in the separation of the *SOX9* promoter from its three enhancer clusters. Together with the finding that SOX9 loss led to the separation of the SOX9-unbound enhancer from both the *MYC* promoter and its SOX9-bound enhancers, these data suggest that promoter-enhancer hubs facilitate enhancer cooperation in setting aberrant expression of *SOX9* and *MYC* in individual TNBC cells. This observation is in line with a recent study reporting that gene expression levels correlate with the sum of the activities of multiple interacting enhancers rather than individual enhancers (*54*). Future work will be needed to determine how the intricacy of multiway enhancer gene regulation can be exploited for diagnosis and anticancer therapy.

Notably, our findings revealed marked variability in hub configurations among individual alleles within each cell population. Even in cells with high *SOX9* expression, interactions between the *SOX9* promoter and enhancer clusters were absent in nearly half of the alleles. In addition, multiway interactions at the *SOX9* and *MYC* loci were relatively rare, further supporting the hypothesis that hubs do not form stable structures but rather are highly dynamic and transient topological assemblies (*34*, *55*–*57*). These findings suggest a model where promoter-enhancer hubs are facilitated by cohesin-mediated loop extrusion, a dynamic and well-described mechanism that has been proposed to facilitate CTCF-mediated structural loops (*58*). This is further corroborated by the appearance of stripes in the ensemble contact maps of *SOX9* (fig. S3B) and *MYC* loci (fig. S6E). As our understanding of promoter-enhancer hubs continues to evolve, future research could expand and leverage super-resolution live imaging technologies that allow the examination of multiple regulatory elements and transcription factors to elucidate the dynamics of promoter-enhancer hub formation at single-allele resolution.

Our combinatorial approach, which integrated multiple genomic and imaging data modalities, has been instrumental in identifying essential promoter-enhancer hubs in TNBC. This approach has also helped elucidate the regulation and organizational principles of *SOX9* and *MYC* spatial hubs in individual cells, offering a potential venue for studying the organization of other spatial hubs and identifying their regulators. Together, our investigation sets the stage for continued exploration in this emerging field and highlights that promoter-enhancer hubs are dynamic topological assemblies, which can be exploited by oncogenic transcription factors to promote aberrant gene expression in a cancer subtype-restricted manner.

MATERIALS AND METHODS
Experimental procedures
Cell culture
The cell lines MB157 (CRL-7721), MDA-MB-468 (HTB-132), and human embryonic kidney (HEK) 293T (CRL-11268) were obtained from the American Tissue Culture Collection (American Type Culture Collection). All cell lines were grown in Dulbecco's modified Eagle's medium (DMEM; Corning, catalog no. 10-013-CV) supplemented with 10% fetal bovine serum (Hyclone, catalog no. SH30070.03), penicillin/streptomycin (100 U/ml and 100 μg/ml; Corning, catalog no. 30-002-CI), and 2 mM L-glutamine (Corning, catalog no. 25-005-CI). When passaging, all cell lines except HEK293T were detached with 0.25% EDTA-free trypsin (Gibco, catalog no. 15090-046) to avoid activation of Notch signaling. HEK293T cells were detached with 0.05% EDTA-free trypsin. All cell lines, including the Cas9-expressing, dCas9-expressing, and pInd-dnMAML–expressing cell lines described below, were grown at 37°C and 5% CO_2 and were used at a low passage number (<12) and subjected to regular mycoplasma tests and short tandem repeat profiling.

Lentiviral packaging
For all dCas9-KRAB and CRISPR-Cas9 experiments using one sgRNA, lentivirus was produced in HEK293T cells as previously described (*6*). Briefly, 4.5×10^6 HEK293T cells were plated in 10 ml of DMEM media in 10-cm dishes 12 to 16 hours before transfection. The lentiviral constructs, packaging plasmid (pCMVdelta), and envelope plasmid (VSV-G) were cotransfected using FuGene HD (Promega, catalog no. E2311). The cells were returned to the incubator, and the cell media were replaced with 6 ml of fresh DMEM media 6 to 8 hours later. Lentiviral supernatants were harvested 48 hours posttransfection, subjected to 0.45-μm filtration, and stored at −80°C.

For the transcription factor CRISPR screen sgRNA pooled library, lentivirus was produced by transfecting HEK293T cells with helper plasmids (VSVG and psPAX2; Addgene: #12260) using FuGene HD (Promega, catalog no. E2311). Briefly, 10 μg of plasmid DNA, 5 μg of VSVG, 7.5 μg of psPAX2, and 26 μl of FuGene HD (Promega, catalog no. E2311) were mixed, incubated, and added to the 10-cm plate of HEK293T cells, and media was replaced 6 to 8 hours posttransfection. Virus was collected 48 and 72 hours posttransfection, subjected to 0.45-μm filtration, and stored at −80°C.

CRISPR-Cas9 and dCas9-KRAB editing
CRISPR-Cas9 system was used for transcription factor CRISPR screen, and genomic deletion of SOX9 and dCas9-KRAB system was used to inactivate *SOX9* enhancers and promoter. Codon-optimized version of Cas9 (Addgene, catalog no. 108100) and dCas9-KRAB (provided by J. Shi) carrying puromycin resistance gene (Cas9-puro and dCas9-KRAB–puro, respectively) and sgRNA vectors carrying GFP (LRG2.1) (*59*) were used. MB157, MDA-MB-231, MDA-MB-468, and MCF7 were transduced with either Cas9-puro or dCas9-KRAB–puro lentivirus by spin infection at 2000 rpm for 90 min at 22°C in the presence of polybrene (6 μg/ml; Sigma-Aldrich, catalog no. H9268). Cells were then returned to the incubator, and media was replaced 12 hours after spin infection. All

cell lines were selected with incremental puromycin 72 hours after spin infection. Transduced MB157 and MCF7 were selected with incremental puromycin (1 to 2 μg/ml) until most cells are viable and maintained in 2 μg/ml. Transduced MDA-MB-468 were selected with puromycin (0.25 μg/ml) and maintained with 0.5 μg/ml. Transduced MDA-MB-231 were selected with 0.5 μg/ml and maintained with 1 μg/ml. The expression of Cas9 was confirmed with Western blot (Cell Signaling Technology, catalog no. 14697S).

sgRNA targeting transcription factors in the human genome used in the CRISPR screen were manually curated on the basis of the presence of DNA binding domain(s). The sgRNAs were designed as previously described (60). This transcription factor DNA binding domain CRISPR sgRNA pooled library is available through Addgene.

sgRNAs targeting SOX9 DNA binding domain and SOX9 enhancers were designed with UCSC genome browser CRISPR Targets Track and Benchling (https://benchling.com/). A total of eight, three, three, and nine sgRNAs were designed for *SOX9*, *SOX9*.EC1, *SOX9*.EC2, and *SOX9*.EC3, respectively. All sgRNAs were cloned into LRG2.1 tagged with GFP: SOX9 targeting sgRNA: CGCCTGCGCCCACAC-CATGA; *SOX9*.E1 targeting sgRNA: TGAGGGTGCAAATTCCA-CAG; *SOX9*.E2 targeting sgRNA: GTAATGGACGGGAGGCACAG; *SOX9*.E3 targeting sgRNA: AAATAAGTCAGGTGTACCAG. In control condition, Cas9- or dCas9-KRAB–expressing cells were transduced with LRG2.1 with nontargeting sgRNA tagged with GFP. Cells were then sorted on a MoFlo Astrios sorter with 100-μm nozzle gating for live cells with 4′,6-diamidino-2-phenylindole (DAPI) staining and top 50% GFP expression.

For targeting SOX9 DNA binding domain, Cas9-expressing MB157, MDA-MB-231, MDA-MB-468, and MCF7 were transduced with lentivirus produced with LRG2.1-SOX9-g10 tagged with GFP using the spin infection method described above. For targeting *SOX9* enhancers, dCas9-KRAB–expressing MB157, MDA-MB-231, MDA-MB-468, and MCF7 were transduced with lentivirus produced with their respective sgRNA using spin infection. The efficacy of SOX9 targeting sgRNA was determined by Tracking of Indels by Decomposition assay and Western blot with an antibody against SOX9 (EMD Millipore, AB5535). The efficacy of SOX9 enhancer targeting sgRNA was determined by quantitative reverse transcription polymerase chain reaction (PCR) using primers for SOX9.

Cloning of domain-focused sgRNA pooled library
The PCR amplified the transcription factor sgRNA pooled library. Cloning of the domain-focused sgRNA pooled library was performed as previously described (60). Briefly, PCR-amplified products were cloned into BsmB1-digested LRG2.1 vector. Plasmids were then electroporated into MegaX DH10B T1R electrocompetent cells.

Pooled CRISPR negative selection screen
CRISPR-based negative selection screenings were performed in MB157 and MDA-MB-468 with stable Cas9 expression. Lentivirus of pooled sgRNA library targeting transcription factor DNA binding domain was produced as described above. To ensure a single-copy sgRNA transduction per cell, multiplicity of infection was set to 0.3 to 0.4. To maintain the representation of sgRNAs during the screen, the number of sgRNA positive cells was kept at least 1000 times the sgRNA number in the library. A portion of the cells were harvested at day 3 postinfection and served as a reference representation of the pooled sgRNA library. Cells were cultured for 15 additional days or approximately five population doublings and harvested as the final time point. Genomic DNA was extracted using a QIAamp DNA mini kit (QIAGEN) according to the manufacturer's instructions.

To quantify the sgRNA abundance of reference and end time points, the sgRNA cassette was PCR-amplified from genomic DNA using high-fidelity polymerase (Phusion master mix, catalog no. F531S). The PCR product was end-repaired by T4 DNA polymerase (New England Biolabs, B02025), DNA polymerase I, large (Klenow) gragment (New England Biolabs, M0210L), and T4 polynucleotide kinase (New England Biolabs, M0201L). Next, a 3′ A-overhang was then added to the ends of blunted DNA fragments with Klenow fragment (3′-5′ exo-) (New England Biolabs, M0212L). The DNA fragments were ligated to diversity-increased custom barcodes with a Quick ligation kit (New England Biolabs, M2200L). Illumina paired-end sequencing adaptors were attached to the barcoded ligated products through PCR reaction with high-fidelity polymerase (Phusion master mix, catalog no. F531S). The final product was quantified by Agilent 4150 TapeStation (Agilent, G2992AA) and pooled together in equal molar ratio and pair-end sequenced by using NextSeq (Illumina) with the NextSeq 500/550 High Output Reagent Kit v2 400-cycle (Illumina) on NextSeq 550.

The sequencing data were demultiplexed and trimmed to contain only the sgRNA sequence cassettes. The read count of each individual sgRNA was calculated with no mismatches and compared to the sequence of reference sgRNA as described previously (61). Individual sgRNAs with the read count lower than 50 in the initial time point were discarded, and the remaining sgRNA counts were normalized to the total sample read counts. MaGeCK was used to identify negatively selected transcription factors using the default settings (62).

Publicly available cancer dependency data from DepMap CRISPRGeneDependency.csv (https://depmap.org/portal/download/all/) were used to construct a heatmap of gene "essentiality" scores across four breast cancer subtypes (<0 = more essential). Rows are ordered by ascending row sum of dependency scores in basal (A/B) subtype. Cumulative distribution functions (CDFs) of essentiality scores were calculated from values displayed in fig. S1G heatmap. Visualization was done in R.

Ectopic induction of dominant negative MAML
dnMAML-GFP was produced by PCR from TetOn-dnMAML-GFP plasmid provided by I. Maillard. The construct was then cloned into pDONR221 with attP1/2 using Gateway cloning BP reactions (Invitrogen, catalog no. 11789020) to produce pDONR221-dnMAML-GFP. pInducer20 (Addgene, catalog no. 44012) was then used with pDONR221-dnMAML-GFP in LR reactions (Invitrogen, catalog no. 11791020) to produce pInducer20-dnMAML-GFP (pInd-dnMAML). All plasmids were subjected to Sanger sequencing validation using Genewiz (https://genewiz.com/). MB157 cells were transduced with lentivirus produced with pInd-dnMAML and selected under G418 (1.25 mg/ml; Gibco, catalog no. 10131027) for 7 days. To ectopically express dnMAML-GFP, DOX (1 μg/ml) was added for 72 hours and replenished after 48 hours. DOX-treated (+DOX) or nontreated (control) cells were then sorted on a MoFlo Astrios sorter with 100-μm nozzle gating for live cells with DAPI staining. DOX-treated MB157-pInd-dnMAML cells were then sorted on the basis of top 50% GFP expression.

RNA sequencing
Around 100,000 cells were washed once with 1× phosphate-buffered saline (PBS) before resuspending pellet in 350 μl of Buffer RLT Plus (QIAGEN) with 1% 2-mercaptoethanol (Sigma-Aldrich) and vortexed

briefly. Subsequently, total RNA was isolated using the RNeasy Plus Micro Kit (QIAGEN). RNA integrity numbers were determined using Agilent 4150 TapeStation (Agilent, G2992AA), and all samples used for RNA sequencing (RNA-seq) library preparation had RNA integrity number greater than 9. Libraries were prepared using the SMARTer Stranded Total RNA-seq Kit v2- Pico Input Mammalian kit (Takara). Three technical replicates were generated for each experiment. Libraries were validated for quality and size distribution using Agilent 4150 TapeStation (Agilent, G2992AA). Libraries were paired-end sequenced (38 bp + 38 bp) with the NextSeq 500/550 High Output Reagent Kit v2 400-cycle (Illumina) on a NextSeq 550 (Illumina).

Chromatin immunoprecipitation sequencing
ChIP-seq was performed as previously described (6). Briefly, chromatin samples prepared from an appropriate number of fixed cells (10^7 for histone modifications and 4×10^7 for transcription factors) were sonicated and cleared with recombinant protein G–conjugated Agarose beads (Invitrogen, catalog no. 15920-010) and subsequently immunoprecipitated with antibodies recognizing H3K27ac (Active Motif, catalog no. 39133), H3K9me3 (Active Motif catalog no. 39161), and SOX9 (EMD Millipore, AB5535). Antibody-chromatin complexes were captured with recombinant protein G–conjugated Agarose beads, washed with low-salt wash buffer, high-salt wash buffer, LiCl wash buffer, and TE buffer with 50 mM NaCl and eluted. Input sample was prepared by the same approach without immunoprecipitation. After reversal of cross-linking, ribonuclease (RNase; Roche, catalog no. 10109169001) and proteinase K (Invitrogen, catalog no. 25530-049) treatments were performed, and DNA was purified with the QIAquick PCR Purification Kit (QIAGEN, catalog no. 28106). Libraries were then prepared using the NEBNext Ultra II DNA library Prep Kit for Illumina (New England Biolabs, catalog no. E7645S). Two replicates were performed for each condition for all experiments except dCas9-KRAB–mediated SOX9 enhancer inactivation experiments, where one replicate was performed. Indexed libraries were validated for quality and size distribution using a TapeStation 2200 (Agilent). Single-end sequencing (75 bp) or paired-end sequencing (38 bp + 38 bp) was performed on a NextSeq 550.

ChIP-seq for Flag was performed as previously described (18). Briefly, Dynabeads Protein G (Thermo Fisher Scientific, catalog no. 10003D) was incubated with antibodies recognizing Flag (NETA/Sigma-Aldrich, catalog no. F1804-5MG) for 8 to 12 hours in PBS + 0.5% bovine serum albumin at 4°C. A total of 4×10^7 cells were cross-linked with 1% formaldehyde and 1.5 mM EGS (Thermo Fisher Scientific, catalog no. 21565) and sonicated using a Brandson 450 sonicator with 17% amplitude, 10-s on, 1-min off for 10 times. Lysate was then cleared by centrifuging for 5 min at 16g, 4°C, and incubated with antibody-bound beads and 1% Triton X-100 (Roche, catalog no. 10789704001) overnight at 4°C. Buffers in all steps above were supplemented with protease inhibitors (Roche, catalog no. 11697498001). Antibody-chromatin complexes captured on beads were then separated on magnet, washed with wash buffer 1, 2, and 3, LiCl wash buffer, and TE buffer, and eluted. Following elution of transcription factor samples, RNase (Roche, catalog no. 10109169001) and proteinase K (Invitrogen, catalog no. 25530-049) treatments were performed and reverse cross-linked at 65°C overnight. DNA was purified with the QiaQuick PCR Purification Kit (QIAGEN, catalog no. 28106). Libraries were then prepared using the NEBNext Ultra II DNA library Prep Kit for Illumina (New England Biolabs,

catalog no. E7645S) with single (New England Biolabs, catalog nos. E7335 and E7710) or dual (New England Biolabs, catalog nos. E7600 and E7780) indexing. Two replicates were performed for each condition. Indexed libraries were validated for quality and size distribution using a TapeStation 4150 (Agilent), quantified by the KAPA Library Quantification Kit (Roche, catalog no. KK4824), and paired-end sequenced (38 bp + 38 bp) on Illumina NextSeq 550.

Cut&Run
Cut&Run experiments were performed using CUTANA ChIC/CUT&RUN Kit 48 rnx (CUTANA, #14-1048) according to the manufacturer's instructions version 3.5. Briefly, Cas9-expressing MB157 cells were spin-infected with Ctrl or SOX9-targeting sgRNA as described in the "CRISPR-Cas9 and dCas9-KRAB editing" section. GFP-positive cells were fluorescence-activated cell sorting–sorted 4 days posttransfection, and nuclei were extracted according to the manufacturer's instructions. Nuclei integrity was examined under light microscopy and immediately proceeded with activated ConA bead binding and antibody binding. One hundred thousand nuclei and 1 μl of H3K27ac antibody (Active Motif, #39133) were used per replicate and incubated overnight at 4°C with nutation. Following binding of pAG-MNase and targeted chromatin digestion and release, purified DNA was quantified with a Qubit 4 fluorometer. Library preparation was performed using the NEBNext Ultra II DNA Library Prep Kit for Illumina (New England Biolabs, #E7645L) with modifications included in the CUTANA protocol. Final libraries were quantified with TapeStation (Agilent, #5067-5583) and KAPA (Roche, #KK4824) and paired-end sequenced on NextSeq 500/550.

High-throughput 3D DNA-FISH
Generation of Oligopaint FISH probes
Oligopaint libraries were designed using the OligoMiner pipeline. Fifty nucleotide sequences with homology to the regions of interest were mined from the hg38 genome build using the default parameters of OligoMiner. Each probe library targeted a 50-kb region of sequence. DNA secondary oligos conjugated with Alexa-488, Atto-565, and Alexa-647 were purchased from Integrated DNA Technologies (IDT) with high-performance liquid chromatography purification. Probe amplification primers and bridges were purchased from IDT with standard desalting.

Oligopaint FISH on slides
Cells were attached to poly-L-lysine–treated glass slides using cytocentrifuge at 1200 rpm for 5 min. Cells were subsequently fixed for 10 min with 4% formaldehyde in PBS at room temperature (RT), followed by membrane permeabilization with 0.5% Triton X-100 in PBS for 15 min at RT. Cells were then washed in 2× SSCT/50% formamide (0.3 M NaCl, 0.03 M sodium citrate, and 0.1% Tween 20) for 5 min, predenatured in 2× SSCT/50% formamide at 92°C for 2.5 min, and then in 2× SSCT/50% formamide at 60°C for 20 min. Ten picomoles of primary Oligopaint probes in hybridization buffer (10% dextran sulfate/2× SSCT/50% formamide/4% polyvinylsulfonic acid/1.4 mM deoxynucleoside triphosphates) was then added to the cells, covered with a coverslip, and sealed with rubber cement. Cells were denatured by placing slides on a heat block in a water bath set to 92°C for 2.5 min, and slides were then transferred to a humidified chamber and incubated overnight at 37°C. Approximately 16 to 18 hours later, coverslips were removed with a razor blade, and slides were washed in 2× SSCT at 60°C for 15 min, 2× SSCT at RT for 10 min, and 0.2× SSC at RT for 10 min. Secondary probes

(10 pmol/25 µl) containing fluorophores (*63*) were added to slides, resuspended again in hybridization buffer containing only 10% formamide, and covered with a coverslip sealed with rubber cement. Slides were incubated at room temperature for 2 hours in a humidified chamber, followed by washes in 2× SSCT at 60°C for 5 min, 2× SSCT at RT for 5 min, and 0.2× SSC at RT for 5 min. All slides were washed with DAPI DNA stain (1:10,000 in PBS) for 5 min, followed by 2× 5-min washes in PBS before mounting in SlowFade Gold Antifade Mountant (Invitrogen, catalog no. S36936).

Cell proliferation
Cell proliferation was measured with the CellTiter Glo Luminescent Cell Viability Assay (Promega, catalog no. G7571) according to the manufacturer's instructions. Cas9-expressing MB157, MDA-MB-468, MDA-MB-231, and MCF7 cells were transduced with control sgRNA or SOX9-targeting sgRNA for 4 days before being isolated by sorting as stated above. Control and SOX9 enhancer inhibited dCas9-expressing MB157, MDA-MB-468, MDA-MB-231, and MCF7 cells were transduced with control sgRNA or SOX9 enhancer targeting sgRNA for 6 days before being isolated by sorting. Cells were then plated in five replicates with 1500, 1500, 1000, and 2000 cells per well in 96-well plates, respectively. Luminescence was first measured 5 hours after plating (day 0) and every 3 days for a total of 9 days. Statistics for cell growth changes were calculated using Student's *t* test.

Quantitative RT-PCR
Primers were designed using Primer-BLAST software. RNA was extracted with the RNeasy Plus Micro Kit (QIAGEN, catalog no. 74034) and synthesized to cDNA with SuperScript III (Invitrogen, catalog no. 18080093). Quantitative PCR was performed on an Applied Biosystem ViiA 7 real-time PCR System using Power SYBR Green PCR Master Mix (Applied Biosystems, catalog no. 4367659). Relative expression level was calculated by the $2^{-(\Delta\Delta Ct)}$ method using *EEF1A1* as internal control for MB157 for MDA-MB-468, MDA-MB-231, and MCF7. Statistics was calculated using a Student's *t* test. *FOXC1* forward: TCACAGAGGATCGGCTTGAAC; *FOXC1* reverse: GTTCGGCTTTGAGGGTGTGT; *SOX9* forward: AGTACCCGCACTTGCACAAC; *SOX9* reverse: CGTTCTTCAC-CGACTTCCTC; *MYC* forward: ACCCTCTCAACGACAGCAGC; *MYC* reverse: ACTCCGTCGAGGAGAGCAGA; *EEF1A1* forward: TTGTCGTCATTGGACACGTAG; *EEF1A1* reverse: TGCCAC-CGCATTTATAGATCAG; *NRARP* forward: AGTCGCTGCTG-CAGAACAT; *NRARP* reverse: AACAGCTTCACCAGCTCCAG; *HEY1* forward: GGTACCCAGTGCCTTTGAGA; *HEY1* reverse: ACCCCAAACTCCGATAGTCC.

Western blot
A total of 0.2 to 1×10^6 cells were washed in ice-cold 1× PBS and lysed with whole lysis buffer (2% SDS and 60 mM tris). Protein concentration was determined with the DC Protein Assay Reagents Package (Bio-Rad, catalog no. 5000116), and 5 to 20 µg of proteins were used for SDS–polyacrylamide gel electrophoresis in tris-messds running buffer (GenScript, catalog nos. M00654 and M00677). Gels were then transferred to methanol activated polyvinylidene difluoride membrane (Cytive, catalog no. 10600023), blocked with 5% skim milk in 1× TBST at room temperature for 1 hour, and incubated with primary antibodies at 1:1000 to 1:20,000 dilutions in 5% skim milk at 4°C overnight. After washing with 1× TBST, 3 × 10min, secondary antibodies (Millipore, catalog nos. 401315-2ml and 401215-2ml) were added at 1:3000 or 1:6000 dilution in 5% skim milk and incubated at room temperature for 1 hour. Following 3 × 15 min wash in 1× TBST, imaging was done with ECL Prime Western Blotting Detection Reagents (Cytiva, catalog no. RPN2232) and autoradiography films.

Quantification and statistical analysis
The statistical significance of differences between measurements was determined by Wilcoxon rank sum test using R (version 3.6.1) wilcox.test function, unless otherwise stated. Statistical details of experiments can be found in figure legends. Visualizations were done with R.

Definition of regulatory elements
The following definitions of regulatory elements were used throughout the manuscript. Promoters: Promoters were defined as ±2.5 kb from the transcription start site (TSS) of each expressed gene. Enhancers: Enhancers were defined as peaks from H3K27ac ChIP-seq greater than 500 bp excluding the ones overlapping with promoters. Enhancer clusters: Enhancer cluster are identical to super-enhancers and were defined by implementing previously described methods (*64*) in R and applying it to H3K27ac peaks.

Regulatory interaction identification/annotation
Significant SMC1 HiChIP interactions were classified as EP, promoter-promoter (PP), or enhancer-enhancer (EE) interactions based on the proximity of each anchor to enhancers and promoters. Promoters were defined as a 5-kb area (±2.5 kb) around the single-nucleotide TSS, and enhancers were also defined as a 5-kb area (±2.5 kb) around the summits of H3K27ac peaks (FDR < 1×10^{-8}) that do not overlap an existing TSS. Active genes are identified via a reads per million per kilobase (RPKM) threshold applied to RNA-seq analysis output. These annotation features are intersected with each HiChIP interaction anchor independently, using findOverlaps() from GenomicRanges R package. Duplicate and self-interactions were discarded from the final set of annotated interactions.

Clique analysis
An undirected graph, with nodes representing enhancers or promoters and edges, the significant EP, PP, and EE interactions between them, was constructed from the annotated significant interactions of SMC1 HiChIP. Communities within this graph were detected via spectral clustering using cluster_louvain() with default parameters from igraph R package. The size of the resulting communities, dubbed "hubs" or "cliques," is represented as the number of edges connecting vertices within that community. Hubs were ranked according to ascending size and plotted according to ranked size. The size cutoff for determining whether a hub is hyper-interacting was previously described (*6*). Briefly, the size cutoff for hyper-interacting hubs was determined by the elbow of rank-ordered hub connectivity count and is visualized by a tangent line at the cutoff. Proportions of genes and enhancers within hyper-interacting hubs were calculated by simple intersections of feature names with lists of each hyper-interacting hubs' member nodes.

To determine the proportion of interactions in hyper/nonhyper-interacting hubs with SOX9 bound to none, one, or both anchors, the GenomicRanges R package was used. The findOverlaps function was used to query overlaps between SOX9 ChIP peaks and the promoters/enhancers participating in hub interactions. Only hubs with at least one anchor overlapping a SOX9 ChIP peak were considered when quantifying proportions of overlap.

To determine the change in interactions in hyper-interacting hubs after GSI treatment, the GenomicRanges R package ("findOverlaps" function) was used to overlap hyper-interacting hub anchors with NCID1 ChIP peaks. Differential loops were determined

as previously described (*6*). Briefly, the criteria for differential contact in MB157 were $\log_2$ FC > 0.5 or < −0.5 and FDR < 1×10^{-10}. Only hubs that were differential, i.e., have at least one changed loop, were considered when quantifying proportions of overlap.

Gene annotation
A total of 2,828,317 Ensembl transcripts in GRCh37.75 assembly were downloaded in gtf format. For each Ensembl gene ID (ENSG), the longest transcript (ENST) was used to assign unique transcriptional start site and gene position. After exclusion of genes annotated as ribosomal RNA or on chromosome M, 57,209 gene annotations were used in RNA-seq analysis.

ChIP-seq data analysis
Alignment
Reads from ChIP-seq for all experiments except SOX9 knockout (KO) and SOX9 enhancer inhibition were trimmed with Trim Galore (version 0.4.1) with parameters -q 15–phred33–gzip–stringency 5 -e 0.1–length 20. Trimmed reads were aligned to the Ensembl GRCh37.75 primary assembly including chromosomes 1 to 22, chrX, chrY, chrM, and contigs using BWA (version 0.7.13) (*65*) with parameters bwa aln -q 5 -l 32 -k 2 -t 6, and paired-end reads were grouped with bwa sampe -P -o 1000000. Reads mapped to contigs, ENCODE blacklist, and marked as duplicates by Picard (version 2.1.0) were discarded, and the remaining reads were used in downstream analyses and visualization.

Reads from H3K27ac and H3K9me3 ChIP-seq in SOX9 enhancer inactivation and H3K27ac Cut&Run in SOX9 KO experiments were trimmed with Trim Galore (version 0.6.10) with parameters -q 15–phred33–gzip–stringency 5 -e 0.1–length 20. Trimmed reads were aligned to the Ensembl GRCh37.75 primary assembly including chromosomes 1 to 22, chrX, chrY, chrM, and contigs using BWA MEM (version 0.7.17) (*65*) with default parameters. Bedtools genomecov was used to count reads over peak regions identified with MACS2 peaks (FDR ≤ 1×10^{-5}). Reads mapped to contigs, ENCODE blacklist, and marked as duplicates by Picard (version 3.1.0) were discarded, and the remaining reads were used in downstream analyses and visualization. DESeq2 then was used to calculated FC and statistical significance of peak regions.

ATAC-seq data analysis
Reads from assay for transposase-accessible chromatin with sequencing (ATAC-seq) experiments were aligned with the same procedure as ChIP-seq described above. Peaks in each sample were identified using MACS with parameters -p 1E-5–nomodel–nolambda–format = BAM -g hs–bw = 300–keep-dup = 1.

RNA-seq data analysis
RNA-seq data were aligned to Ensembl GRCh37.75 primary assembly including chromosomes 1 to 22, chrX, chrY, chrM, and contigs using STAR (version 2.5) (*66*) with parameters –outFilterIntronMotifs RemoveNoncanonicalUnannotated–alignIntronMax 100000–outSAMstrandField intronMotif–outSAMunmapped Within–chimSegmentMin 25 –chimJunctionOverhangMin 25. Strand-specific read counts were quantified using Subread (version 1.5.1) featureCounts with parameters -t exon -g gene_id -s 1 -T 6 and used as input to differential gene expression analysis. Read counts were normalized to RPKM for each gene. Expressed genes were determined as genes with >1 RPKM in all replicates in the control condition.

Differential gene expression analysis in SOX9 KO versus CTRL condition triplicates was performed using DEseq2 with parameters test = "Wald," betaPrior = F, fitType = "parametric." In MB157, genes that showed $\log_2$ FC > 0.5 or < −0.5 with FDR < 0.05 were considered differentially expressed. Genes down-regulated in SOX9 KO, i.e., $\log_2$ FC < −0.5 were considered SOX9-dependent genes.

Expressed genes in MB157 CTRL and SOX9 KO were ranked by $\log_2$ FC and used to conduct gene set enrichment analysis (*67*) in fig. S6B with 100,000 permutations against hallmark gene sets (H), curated gene sets (C2), and oncogenic signature gene sets (C6) from Molecular Signatures Database (version 6.1) (*67*). Visualization was done in R.

RNA-seq data for MDA-MB-468 were downloaded from Gene Expression Omnibus (SRA: SRX6666590). *SOX9* expression in primary human tumors and normal tissue was derived from RNA-seq data obtained from The Cancer Genome Atlas (TCGA) database and were visualized with GEPIA2. *MYC* expression in SOX9-high and SOX9-low primary human tumors was derived from TCGA database and analyzed using XENA.

Sequencing data visualization
ChIP-seq and RNA-seq tracks
Bedgraph of reads normalized to reads per million from ChIP-seq and RNA-seq was generated with bedtools genomecov. Selected genomic loci were visualized with R package Sushi (version 1.18.0) function "plotBedgraph." Genome-wide uploadable bigWig files were generated with UCSC tools (version 329) (*68*) "bedGraphToBigWig." Normalized ChIP-seq tracks for MDA-MB-468, MDA-MB-231, MCF7, LTED, and primary human luminal progenitor cells were downloaded from Cistrome.

Hi-ChIP contact map
SMC1 HiChIP data were stored in ".mcool" format and was corrected via vanilla-coverage square-root normalization and plotted at 10-kb resolution in a pyramid style using the GENOVA "pyramid()" function.

DNA-FISH imaging and analysis
Prepared cells were imaged on a Leica TCS SP8 Multiphoton Confocal using a 40× HC PL APO 1.3–numerical aperture oil immersion objective with pixels of 135 × 135 nm and *z* spacing of 350 nm. We obtained stacks representing 10.5 μm in total axial thickness. Image analysis was performed with the TANGO package in FIJI. Raw images were processed with Fast Filters 3D and Misc 3D filters before Simple Segmenter with the OTSU method was used to segment nuclei. Nuclei were then manually checked to eliminate any that were not intact. Probes were then processed with Fast Filters 3D, Misc 3D Filters, and Subtract Background 2D, and the brightest 0.35% of fluorescence was segmented. 3D Euclidian distances from the center of the nearest neighboring probes in each pair of channels were then calculated. For two-color FISH analyses, alleles were only kept if both probes were present (having a 3D Euclidian distance of <2.5 μm). For three-color FISH analyses, alleles were only kept if all three probes were present (having a 3D Euclidian distance of <2.5 μm between any two pairs of probes). The spatial perimeter between three probes was defined as the sum of the 3D Euclidean distances between probe 1 to probe 2, probe 2 to probe 3, and probe 1 to probe 3 for each allele.

Supplementary Materials
This PDF file includes:
Figs. S1 to S7
Legends for tables S1 to S3

Other Supplementary Material for this manuscript includes the following:
Tables S1 to S3

REFERENCES AND NOTES

1. M. Yu, B. Ren, The three-dimensional organization of mammalian genomes. *Annu. Rev. Cell Dev. Biol.* **33**, 265–289 (2017).

2. A. M. Oudelaar, J. O. J. Davies, L. L. P. Hanssen, J. M. Telenius, R. Schwessinger, Y. Liu, J. M. Brown, D. J. Downes, A. M. Chiariello, S. Bianco, M. Nicodemi, V. J. Buckle, J. Dekker, D. R. Higgs, J. R. Hughes, Single-allele chromatin interactions identify regulatory hubs in dynamic compartmentalized domains. *Nat. Genet.* **50**, 1744–1751 (2018).

3. C. M. Uyehara, E. Apostolou, 3D enhancer-promoter interactions and multi-connected hubs: Organizational principles and functional roles. *Cell Rep.* **42**, 112068 (2023).

4. J. Zhao, R. B. Faryabi, Spatial promoter-enhancer hubs in cancer: Organization, regulation, and function. *Trends Cancer* **9**, 1069–1084 (2023).

5. R. Sanalkumar, R. Dong, L. Lee, Y. H. Xing, S. Iyer, I. Letovanec, S. la Rosa, G. Finzi, E. Musolino, R. Papait, I. Chebib, G. P. Nielsen, R. Renella, G. M. Cote, E. Choy, M. Aryee, K. Stegmaier, I. Stamenkovic, M. N. Rivera, N. Riggi, Highly connected 3D chromatin networks established by an oncogenic fusion protein shape tumor cell identity. *Sci. Adv.* **9**, eabo3789 (2023).

6. J. Petrovic, Y. Zhou, M. Fasolino, N. Goldman, G. W. Schwartz, M. R. Mumbach, S. C. Nguyen, K. S. Rome, Y. Sela, Z. Zapataro, S. C. Blacklow, M. J. Kruhlak, J. Shi, J. C. Aster, E. F. Joyce, S. C. Little, G. Vahedi, W. S. Pear, R. B. Faryabi, Oncogenic Notch promotes long-range regulatory interactions within hyperconnected 3D cliques. *Mol. Cell* **73**, 1174–1190.e12 (2019).

7. Y. Liu, B. Guo, E. Aguilera-Jimenez, V. S. Chu, J. Zhou, Z. Wu, J. M. Francis, X. Yang, P. S. Choi, S. D. Bailey, X. Zhang, Chromatin looping shapes KLF5-dependent transcriptional programs in human epithelial cancers. *Cancer Res.* **80**, 5464–5477 (2020).

8. L. Yang, F. Chen, H. Zhu, Y. Chen, B. Dong, M. Shi, W. Wang, Q. Jiang, L. Zhang, X. Huang, M. Q. Zhang, H. Wu, 3D genome alterations associated with dysregulated HOXA13 expression in high-risk T-lineage acute lymphoblastic leukemia. *Nat. Commun.* **12**, 3708 (2021).

9. J. Xu, F. Song, H. Lyu, M. Kobayashi, B. Zhang, Z. Zhao, Y. Hou, X. Wang, Y. Luan, B. Jia, L. Stasiak, J. H. Y. Wong, Q. Wang, Q. Jin, Q. Jin, Y. Fu, H. Yang, R. C. Hardison, S. Dovat, L. C. Platanias, Y. Diao, Y. Yang, T. Yamada, A. D. Viny, R. L. Levine, D. Claxton, J. R. Broach, H. Zheng, F. Yue, Subtype-specific 3D genome alteration in acute myeloid leukaemia. *Nature* **611**, 387–398 (2022).

10. S. K. Rhie, A. A. Perez, F. D. Lay, S. Schreiner, J. Shi, J. Polin, P. J. Farnham, A high-resolution 3D epigenomic map reveals insights into the creation of the prostate cancer transcriptome. *Nat. Commun.* **10**, 4154 (2019).

11. E. P. Nora, B. R. Lajoie, E. G. Schulz, L. Giorgetti, I. Okamoto, N. Servant, T. Piolot, N. L. van Berkum, J. Meisig, J. Sedat, J. Gribnau, E. Barillot, N. Blüthgen, J. Dekker, E. Heard, Spatial partitioning of the regulatory landscape of the X-inactivation centre. *Nature* **485**, 381–385 (2012).

12. E. Lieberman-Aiden, N. L. van Berkum, L. Williams, M. Imakaev, T. Ragoczy, A. Telling, I. Amit, B. R. Lajoie, P. J. Sabo, M. O. Dorschner, R. Sandstrom, B. Bernstein, M. A. Bender, M. Groudine, A. Gnirke, J. Stamatoyannopoulos, L. A. Mirny, E. S. Lander, J. Dekker, Comprehensive mapping of long-range interactions reveals folding principles of the human genome. *Science* **326**, 289–293 (2009).

13. J. R. Dixon, S. Selvaraj, F. Yue, A. Kim, Y. Li, Y. Shen, M. Hu, J. S. Liu, B. Ren, Topological domains in mammalian genomes identified by analysis of chromatin interactions. *Nature* **485**, 376–380 (2012).

14. P. Vangala, R. Murphy, S. A. Quinodoz, K. Gellatly, P. McDonel, M. Guttman, M. Garber, High-resolution mapping of multiway enhancer-promoter interactions regulating pathogen detection. *Mol. Cell* **80**, 359–373.e8 (2020).

15. A. Allahyar, C. Vermeulen, B. A. M. Bouwman, P. H. L. Krijger, M. J. A. M. Verstegen, G. Geeven, M. van Kranenburg, M. Pieterse, R. Straver, J. H. I. Haarhuis, K. Jalink, H. Teunissen, I. J. Renkens, W. P. Kloosterman, B. D. Rowland, E. de Wit, J. de Ridder, W. de Laat, Enhancer hubs and loop collisions identified from single-allele topologies. *Nat. Genet.* **50**, 1151–1160 (2018).

16. K. P. Eagen, C. A. French, Supercharging BRD4 with NUT in carcinoma. *Oncogene* **40**, 1396–1408 (2021).

17. H. Yang, H. Zhang, Y. Luan, T. Liu, W. Yang, K. G. Roberts, M. X. Qian, B. Zhang, W. Yang, V. Perez-Andreu, J. Xu, S. Iyyanki, D. Kuang, L. A. Stasiak, S. C. Reshmi, J. Gastier-Foster, C. Smith, C. H. Pui, W. E. Evans, S. P. Hunger, L. C. Platanias, M. V. Relling, C. G. Mullighan, M. L. Loh, F. Yue, J. J. Yang, Noncoding genetic variation in GATA3 increases acute lymphoblastic leukemia risk through local and global changes in chromatin conformation. *Nat. Genet.* **54**, 170–179 (2022).

18. Y. Zhou, J. Petrovic, J. Zhao, W. Zhang, A. Bigdeli, Z. Zhang, S. L. Berger, W. S. Pear, R. B. Faryabi, EBF1 nuclear repositioning instructs chromatin refolding to promote therapy resistance in T leukemic cells. *Mol. Cell* **82**, 1003–1020.e15 (2022).

19. C. Denkert, C. Liedtke, A. Tutt, G. von Minckwitz, Molecular alterations in triple-negative breast cancer-the road to new treatment strategies. *Lancet* **389**, 2430–2442 (2017).

20. C. Wang, J. R. Christin, M. H. Oktay, W. Guo, Lineage-biased stem cells maintain estrogen-receptor-positive and -negative mouse mammary luminal lineages. *Cell Rep.* **18**, 2825–2835 (2017).

21. W. Guo, Z. Keckesova, J. L. Donaher, T. Shibue, V. Tischler, F. Reinhardt, S. Itzkovitz, A. Noske, U. Zürrer-Härdi, G. Bell, W. L. Tam, S. A. Mani, A. van Oudenaarden, R. A. Weinberg, Slug and Sox9 cooperatively determine the mammary stem cell state. *Cell* **148**, 1015–1028 (2012).

22. G. Domenici, I. Aurrekoetxea-Rodríguez, B. M. Simões, M. Rábano, S. Y. Lee, J. S. Millán, V. Comaills, E. Oliemuller, J. A. López-Ruiz, I. Zabalza, B. A. Howard, R. M. Kypta, M. d. Vivanco, A Sox2-Sox9 signalling axis maintains human breast luminal progenitor and breast cancer stem cells. *Oncogene* **38**, 3151–3169 (2019).

23. T. A. Proia, P. J. Keller, P. B. Gupta, I. Klebba, A. D. Jones, M. Sedic, H. Gilmore, N. Tung, S. P. Naber, S. Schnitt, E. S. Lander, C. Kuperwasser, Genetic predisposition directs breast cancer phenotype by dictating progenitor cell fate. *Cell Stem Cell* **8**, 149–163 (2011).

24. G. Molyneux, F. C. Geyer, F. A. Magnay, A. McCarthy, H. Kendrick, R. Natrajan, A. MacKay, A. Grigoriadis, A. Tutt, A. Ashworth, J. S. Reis-Filho, M. J. Smalley, BRCA1 basal-like breast cancers originate from luminal epithelial progenitors and not from basal stem cells. *Cell Stem Cell* **7**, 403–417 (2010).

25. E. Lim, D. Wu, B. Pal, T. Bouras, M. L. Asselin-Labat, F. Vaillant, H. Yagita, G. J. Lindeman, G. K. Smyth, J. E. Visvader, Transcriptome analyses of mouse and human mammary cell subpopulations reveal multiple conserved genes and pathways. *Breast Cancer Res.* **12**, R21 (2010).

26. E. Lim, F. Vaillant, D. Wu, N. C. Forrest, B. Pal, A. H. Hart, M.-L. Asselin-Labat, D. E. Gyorki, T. Ward, A. Partanen, F. Feleppa, L. I. Huschtscha, H. J. Thorne, kConFab, S. B. Fox, M. Yan, J. D. French, M. A. Brown, G. K. Smyth, J. E. Visvader, G. J. Lindeman, Aberrant luminal progenitors as the candidate target population for basal tumor development in BRCA1 mutation carriers. *Nat. Med.* **15**, 907–913 (2009).

27. J. R. Christin, C. Wang, C. Y. Chung, Y. Liu, C. Dravis, W. Tang, M. H. Oktay, G. M. Wahl, W. Guo, Stem cell determinant SOX9 promotes lineage plasticity and progression in basal-like breast cancer. *Cell Rep.* **31**, 107742 (2020).

28. J. G. Tate, S. Bamford, H. C. Jubb, Z. Sondka, D. M. Beare, N. Bindal, H. Boutselakis, C. G. Cole, C. Creatore, E. Dawson, P. Fish, B. Harsha, C. Hathaway, S. C. Jupe, C. Y. Kok, K. Noble, L. Ponting, C. C. Ramshaw, C. E. Rye, H. E. Speedy, R. Stefancsik, S. L. Thompson, S. Wang, S. Ward, P. J. Campbell, S. A. Forbes, COSMIC: The catalogue of somatic mutations in cancer. *Nucleic Acids Res.* **47**, D941–D947 (2019).

29. L. A. Gilbert, M. A. Horlbeck, B. Adamson, J. E. Villalta, Y. Chen, E. H. Whitehead, C. Guimaraes, B. Panning, H. L. Ploegh, M. C. Bassik, L. S. Qi, M. Kampmann, J. S. Weissman, Genome-scale CRISPR-mediated control of gene repression and activation. *Cell* **159**, 647–661 (2014).

30. S. Xie, J. Duan, B. Li, P. Zhou, G. C. Hon, Multiplexed engineering and analysis of combinatorial enhancer activity in single cells. *Mol. Cell* **66**, 285–299.e5 (2017).

31. E. H. Finn, G. Pegoraro, H. B. Brandão, A. L. Valton, M. E. Oomen, J. Dekker, L. Mirny, T. Misteli, Extensive heterogeneity and intrinsic variation in spatial genome organization. *Cell* **176**, 1502–1515.e10 (2019).

32. V. Roukos, T. C. Voss, C. K. Schmidt, S. Lee, D. Wangsa, T. Misteli, Spatial dynamics of chromosome translocations in living cells. *Science* **341**, 660–664 (2013).

33. M. Gabriele, H. B. Brandão, S. Grosse-Holz, A. Jha, G. M. Dailey, C. Cattoglio, T. H. S. Hsieh, L. Mirny, C. Zechner, A. S. Hansen, Dynamics of CTCF- and cohesin-mediated chromatin looping revealed by live-cell imaging. *Science* **376**, 496–501 (2022).

34. L. F. Chen, H. K. Long, M. Park, T. Swigut, A. N. Boettiger, J. Wysocka, Structural elements promote architectural stripe formation and facilitate ultra-long-range gene regulation at a human disease locus. *Mol. Cell* **83**, 1446–1461.e6 (2023).

35. S. Sungalee, Y. Liu, R. A. Lambuta, N. Katanayeva, M. Donaldson Collier, D. Tavernari, S. Roulland, G. Ciriello, E. Oricchio, Histone acetylation dynamics modulates chromatin conformation and allele-specific interactions at oncogenic loci. *Nat. Genet.* **53**, 650–662 (2021).

36. D. C. Di Giammartino, A. Kloetgen, A. Polyzos, Y. Liu, D. Kim, D. Murphy, A. Abuhashem, P. Cavaliere, B. Aronson, V. Shah, N. Dephoure, M. Stadtfeld, A. Tsirigos, E. Apostolou, KLF4 is involved in the organization and regulation of pluripotency-associated three-dimensional enhancer networks. *Nat. Cell Biol.* **21**, 1179–1190 (2019).

37. A. J. Rubin, B. C. Barajas, M. Furlan-Magaril, V. Lopez-Pajares, M. R. Mumbach, I. Howard, D. S. Kim, L. D. Boxer, J. Cairns, M. Spivakov, S. W. Wingett, M. Shi, Z. Zhao, W. J. Greenleaf, A. Kundaje, M. Snyder, H. Y. Chang, P. Fraser, P. A. Khavari, Lineage-specific dynamic and pre-established enhancer-promoter contacts cooperate in terminal differentiation. *Nat. Genet.* **49**, 1522–1528 (2017).

38. D. H. Phanstiel, K. van Bortle, D. Spacek, G. T. Hess, M. S. Shamim, I. Machol, M. I. Love, E. L. Aiden, M. C. Bassik, M. P. Snyder, Static and dynamic DNA loops form AP-1-bound activation hubs during macrophage development. *Mol. Cell* **67**, 1037–1048.e6 (2017).

39. Y. He, W. S. Pear, Notch signalling in B cells. *Semin. Cell Dev. Biol.* **14**, 135–142 (2003).

40. I. Maillard, S. H. Adler, W. S. Pear, Notch and the immune system. *Immunity* **19**, 781–791 (2003).

41. S. Artavanis-Tsakonas, M. D. Rand, R. J. Lake, Notch signaling: Cell fate control and signal integration in development. *Science* **284**, 770–776 (1999).

42. T. Bouras, B. Pal, F. Vaillant, G. Harburg, M. L. Asselin-Labat, S. R. Oakes, G. J. Lindeman, J. E. Visvader, Notch signaling regulates mammary stem cell function and luminal cell-fate commitment. *Cell Stem Cell* **3**, 429–441 (2008).

43. V. Rodilla, A. Dasti, M. Huyghe, D. Lafkas, C. Laurent, F. Reyal, S. Fre, Luminal progenitors restrict their lineage potential during mammary gland development. *PLoS Biol.* **13**, e1002069 (2015).

44. A. Van Keymeulen, M. Fioramonti, A. Centonze, G. Bouvencourt, Y. Achouri, C. Blanpain, Lineage-restricted mammary stem cells sustain the development, homeostasis, and regeneration of the estrogen receptor positive lineage. *Cell Rep.* **20**, 1525–1532 (2017).

45. M. V. Giuli, E. Giuliani, I. Screpanti, D. Bellavia, S. Checquolo, Notch signaling activation as a hallmark for triple-negative breast cancer subtype. *J. Oncol.* **2019**, 8707053 (2019).

46. K. Miao, J. H. Lei, M. V. Valecha, A. Zhang, J. Xu, L. Wang, X. Lyu, S. Chen, Z. Miao, X. Zhang, S. M. Su, F. Shao, B. K. Rajendran, J. Bao, J. Zeng, H. Sun, P. Chen, K. Tan, Q. Chen, K. H. Wong, X. Xu, C. X. Deng, NOTCH1 activation compensates BRCA1 deficiency and promotes triple-negative breast cancer formation. *Nat. Commun.* **11**, 3256 (2020).

47. I. Maillard, U. Koch, A. Dumortier, O. Shestova, L. Xu, H. Sai, S. E. Pross, J. C. Aster, A. Bhandoola, F. Radtke, W. S. Pear, Canonical notch signaling is dispensable for the maintenance of adult hematopoietic stem cells. *Cell Stem Cell* **2**, 356–366 (2008).

48. Y. Wang, T. Zhang, N. Kwiatkowski, B. J. Abraham, T. I. Lee, S. Xie, H. Yuzugullu, T. von, H. Li, Z. Lin, D. G. Stover, E. Lim, Z. C. Wang, J. D. Iglehart, R. A. Young, N. S. Gray, J. J. Zhao, CDK7-dependent transcriptional addiction in triple-negative breast cancer. *Cell* **163**, 174–186 (2015).

49. G. Barshad, J. J. Lewis, A. G. Chivu, A. Abuhashem, N. Krietenstein, E. J. Rice, Y. Ma, Z. Wang, O. J. Rando, A. K. Hadjantonakis, C. G. Danko, RNA polymerase II dynamics shape enhancer-promoter interactions. *Nat. Genet.* **55**, 1370–1380 (2023).

50. K. A. Nilson, J. Guo, M. E. Turek, J. E. Brogie, E. Delaney, D. S. Luse, D. H. Price, THZ1 reveals roles for Cdk7 in co-transcriptional capping and pausing. *Mol. Cell* **59**, 576–587 (2015).

51. X. Ye, W. L. Tam, T. Shibue, Y. Kaygusuz, F. Reinhardt, E. Ng Eaton, R. A. Weinberg, Distinct EMT programs control normal mammary stem cells and tumour-initiating cells. *Nature* **525**, 256–260 (2015).

52. Y. Yashiro-Ohtani, H. Wang, C. Zang, K. L. Arnett, W. Bailis, Y. Ho, B. Knoechel, C. Lanauze, L. Louis, K. S. Forsyth, S. Chen, Y. Chung, J. Schug, G. A. Blobel, S. A. Liebhaber, B. E. Bernstein, S. C. Blacklow, X. S. Liu, J. C. Aster, W. S. Pear, Long-range enhancer activity determines Myc sensitivity to Notch inhibitors in T cell leukemia. *Proc. Natl. Acad. Sci. U.S.A.* **111**, E4946–E4953 (2014).

53. D. C. Di Giammartino, A. Polyzos, E. Apostolou, Transcription factors: Building hubs in the 3D space. *Cell Cycle* **19**, 2395–2410 (2020).

54. J. Choi, K. Lysakovskaia, G. Stik, C. Demel, J. Söding, T. V. Tian, T. Graf, P. Cramer, Evidence for additive and synergistic action of mammalian enhancers during cell fate determination. *eLife* **10**, e65381 (2021).

55. S. A. Quinodoz, N. Ollikainen, B. Tabak, A. Palla, J. M. Schmidt, E. Detmar, M. M. Lai, A. A. Shishkin, P. Bhat, Y. Takei, V. Trinh, E. Aznauryan, P. Russell, C. Cheng, M. Jovanovic, A. Chow, L. Cai, P. McDonel, M. Garber, M. Guttman, Higher-order inter-chromosomal hubs shape 3D genome organization in the nucleus. *Cell* **174**, 744–757.e24 (2018).

56. K. Kawasaki, T. Fukaya, Functional coordination between transcription factor clustering and gene activity. *Mol. Cell* **83**, 1605–1622.e9 (2023).

57. A. Hafner, M. Park, S. E. Berger, S. E. Murphy, E. P. Nora, A. N. Boettiger, Loop stacking organizes genome folding from TADs to chromosomes. *Mol. Cell* **83**, 1377–1392.e6 (2023).

58. S. Yatskevich, J. Rhodes, K. Nasmyth, Organization of chromosomal DNA by SMC complexes. *Annu. Rev. Genet.* **53**, 445–482 (2019).

59. J. D. Grevet, X. Lan, N. Hamagami, C. R. Edwards, L. Sankaranarayanan, X. Ji, S. K. Bhardwaj, C. J. Face, D. F. Posocco, O. Abdulmalik, C. A. Keller, B. Giardine, S. Sidoli, B. A. Garcia, S. T. Chou, S. A. Liebhaber, R. C. Hardison, J. Shi, G. A. Blobel, Domain-focused CRISPR screen identifies HRI as a fetal hemoglobin regulator in human erythroid cells. *Science* **361**, 285–290 (2018).

60. B. Lu, O. Klingbeil, Y. Tarumoto, T. D. D. Somerville, Y. H. Huang, Y. Wei, D. C. Wai, J. K. K. Low, J. P. Milazzo, X. S. Wu, Z. Cao, X. Yan, O. E. Demerdash, G. Huang, J. P. Mackay, J. B. Kinney, J. Shi, C. R. Vakoc, A transcription factor addiction in leukemia imposed by the MLL promoter sequence. *Cancer Cell* **34**, 970–981.e8 (2018).

61. J. Shi, E. Wang, J. P. Milazzo, Z. Wang, J. B. Kinney, C. R. Vakoc, Discovery of cancer drug targets by CRISPR-Cas9 screening of protein domains. *Nat. Biotechnol.* **33**, 661–667 (2015).

62. W. Li, H. Xu, T. Xiao, L. Cong, M. I. Love, F. Zhang, R. A. Irizarry, J. S. Liu, M. Brown, X. S. Liu, MAGeCK enables robust identification of essential genes from genome-scale CRISPR/Cas9 knockout screens. *Genome Biol.* **15**, 554 (2014).

63. B. J. Beliveau, J. Y. Kishi, G. Nir, H. M. Sasaki, S. K. Saka, S. C. Nguyen, C. T. Wu, P. Yin, OligoMiner provides a rapid, flexible environment for the design of genome-scale oligonucleotide in situ hybridization probes. *Proc. Natl. Acad. Sci. U.S.A.* **115**, E2183–E2192 (2018).

64. W. A. Whyte, D. A. Orlando, D. Hnisz, B. J. Abraham, C. Y. Lin, M. H. Kagey, P. B. Rahl, T. I. Lee, R. A. Young, Master transcription factors and mediator establish super-enhancers at key cell identity genes. *Cell* **153**, 307–319 (2013).

65. H. Li, R. Durbin, Fast and accurate short read alignment with Burrows-Wheeler transform. *Bioinformatics* **25**, 1754–1760 (2009).

66. A. Dobin, C. A. Davis, F. Schlesinger, J. Drenkow, C. Zaleski, S. Jha, P. Batut, M. Chaisson, T. R. Gingeras, STAR: Ultrafast universal RNA-seq aligner. *Bioinformatics* **29**, 15–21 (2013).

67. A. Subramanian, P. Tamayo, V. K. Mootha, S. Mukherjee, B. L. Ebert, M. A. Gillette, A. Paulovich, S. L. Pomeroy, T. R. Golub, E. S. Lander, J. P. Mesirov, Gene set enrichment analysis: A knowledge-based approach for interpreting genome-wide expression profiles. *Proc. Natl. Acad. Sci. U.S.A.* **102**, 15545–15550 (2005).

68. W. J. Kent, A. S. Zweig, G. Barber, A. S. Hinrichs, D. Karolchik, BigWig and BigBed: Enabling browsing of large distributed datasets. *Bioinformatics* **26**, 2204–2207 (2010).